European Journal of Pharmaceutical Sciences 175 (2022) 106226

Contents lists available at ScienceDirect

European Journal of Pharmaceutical Sciences

journal homepage: www.elsevier.com/locate/ejps

Capsule-Based dry powder inhaler evaluation using CFD-DEM simulations and next generation impactor data

Lucilla C. Almeida [a], Rahul Bharadwaj [a], Avi Eliahu [b], Carl R. Wassgren [c], Karthik Nagapudi [d], Ariel R. Muliadi [*,d]

[a] *Engineering Simulation and Scientific Software, ESSS, Rua Orlando Phillipi, 100, Florianopolis, SC 88032-700, Brazil*
[b] *Device Development, Genentech Inc., 1 DNA Way, South San Francisco, California 94080, USA*
[c] *School of Mechanical Engineering, Purdue University, 585 Purdue Mall, West Lafayette, Indiana 47907-2088, USA*
[d] *Small Molecule Pharmaceutics, Research & Early Development (gRED), Genentech Inc., 1 DNA Way, South San Francisco, California 94080, USA*

ARTICLE INFO

Keywords:
CFD-DEM
Dry powder inhalers
Discrete element method
Computational fluid dynamics
Inhalation drug delivery

ABSTRACT

Capsule-based, single-dose dry powder inhalers (DPIs) are commonly-used devices to deliver medications to the lungs. This work evaluates the effect of the drug/excipient adhesive bonding and the DPI resistances on the aerosol performance using a combination of empirical multi-stage impactor data and a fully-coupled computational fluid dynamics (CFD) and discrete element method (DEM) model. Model-predicted quantities show that the primary modes of powder dispersion are a function of the device resistance. Lowering the device resistance increases its capacity to transport a wider range of particle size classes toward the outlet and generate more intense turbulence upstream therein. On the other hand, a higher device resistance increases the velocity of the tangential airflow along the device walls, which in turn increases the intensity of particle/device impaction. Correlating model data and experimental results shows that these differing powder dispersion mechanisms affect different formulations differently, with finer aerosols tending to result when pairing a lower resistance device with formulations that exhibit low API/excipient adhesion, or when pairing a high resistance device with more cohesive formulations.

1. Introduction

1.1. *Dry powder inhalers*

Direct delivery of drugs to the target organ allows for the local concentration to be maximized while at the same time minimizing the systemic concentration. This in turn, can potentially increase efficacy and mitigate/eliminate side effects associated with systemic delivery. Thus, Pulmonary drug delivery has emerged as an effective therapeutic route for the treatment of respiratory diseases. As an added benefit, the absence of the first-pass metabolism in the lung also paves the way for delivery of large molecules (e.g., antibiotics, peptides, etc.) in high doses. In addition, it has also been demonstrated that specific systemic immune responses can be triggered following certain inhaled therapies, making them a potential route for vaccine administration (Staquicini et al., 2021).

Inhaled therapeutics are normally delivered through the use of a metered-dose inhaler (MDI) or a dry powder inhaler (DPI). Unlike MDIs, which rely on a metering valve and propellant to portion out a prescribed amount of aerosolized dose from a drug reservoir, DPIs are breath-actuated, i.e., they rely on the airflow generated by inhalation to evacuate and aerosolize a drug that is prepackaged in individual (unit) dose containers. Moreover, as solid formulations are used in DPIs, they can provide the advantage of improved physical and chemical stability of the drug when compared to MDIs, which use solution or suspension formulations.

DPIs can be grouped into two main device categories: single (unit) dose and multi-unit dose. The former category contains only one dose at any given time. Here, the drug or drug product is normally contained in a standard size-2 or size-3 hard-shell capsule that must be manually placed into the device prior to each use. The latter type is preloaded with one or two strips of prefilled, individually sealed foil-laminated blisters that supply multiple days' worth of doses. As the amount of drug that can be delivered through each inhalation is limited mostly by the size of the unit dose container, capsule-based DPIs are more suitable for the delivery of high-dose inhaled therapeutics (de Boer et al., 2017). For either device type, some built-in mechanics must be operated to pierce

---

* Corresponding author.
E-mail address: muliadi.ariel@gene.com (A.R. Muliadi).

https://doi.org/10.1016/j.ejps.2022.106226
Received 2 March 2022; Received in revised form 3 May 2022; Accepted 23 May 2022

Nomenclature

s	Contact overlap
L	Particle size
d	diameter
u	fluid velocity component
v	Particle velocity component
C_D	Drag coefficient
C_L	Lift coefficient
C_{VM}	Virtual mass coefficient
K	Stiffness
E	Elastic (Young's) modulus
F	Force component
A'	Particle projected area in the direction of the flow
t	Time
p	Pressure
f	Drag function
Re	Reynolds number
m	Mass
A	Area
T	Temperature
$\dot{q}$	Heat transfer rate
h	Averaged convective heat transfer coefficient
c	Material specific heat
Nu	Nusselt number
Sh	Sherwood number
Pr	Prandt number
k	Thermal conductivity
h	Enthalpy
Q	Heat source
q	Heat exchanged by particle and fluid
H	Contact conductance
r	Radius
E	Relative error
R	External radius of the particle
q''	Conductive flux
c	Contact
H	Contact home particle
N	Contact near particle
f	Fluid
p	Particle
nl	Loading contact step
nu	Unloading contact step
o	Previous time step
n	Normal component
τ	Tangential component
r	Relative
i	Interfacial
s	Solid phase
C	Cell
VM	Virtual mass
L	Lift
D	Drag
N-D	Non-drag
d	Dynamic
st	Static
B	Buoyancy
eff	Effective
Δ	Averaging radius
S	Surface
av	Average
0	Center
e	elastic
$t-\Delta t$	Previous time step
t	Current time step
$\boldsymbol{n}$	Contact plane unit normal vector
$\boldsymbol{x}$	Position vector
$\boldsymbol{\omega}$	Angular velocity vector
$\boldsymbol{F}$	Force
$\boldsymbol{g}$	Gravity vector
$\boldsymbol{a}$	Acceleration vector
$\boldsymbol{I}$	Identity tensor
$\boldsymbol{J}$	Moment of inertia
$\boldsymbol{M}$	Net torque
$\boldsymbol{q}$	Heat flux
β	Momentum exchange coefficient
α	Volume Fraction
ρ	Density
μ	Shear viscosity
ε	Restitution coefficient
$\mathbb{T}$	Stress-strain tensor
τ	Response time
ϕ	Sphericity
χ	Ratio of Re_r and Re_G
λ	Bulk viscosity
η	Friction coefficient
σ	Poisson ratio
ϵ	Void fraction
U	Superficial Velocity
α	Cell porosity
m_p	Particle mass
p	Particle mass
d_p	Particle diameter
A_{p_p}	Particle area
ρ_p	Particle density
α_p	Particle volume fraction
Re_p	Particle Reynolds numbers
$\boldsymbol{v}_p$	Particle velocity vector
$\boldsymbol{\omega}_p$	Particle angular velocity
$\boldsymbol{J}_p$	Particle moment of inertia
$\boldsymbol{v}_p$	Force due to contact
$\boldsymbol{F}_{f\to p}$	Force acting on particle due to the fluid phase
$\boldsymbol{M}_{f\to p}$	Net torque due to the fluid phase
$\boldsymbol{M}_c$	Net torque due to contacts
$\boldsymbol{F}_n$	Normal force
$\boldsymbol{F}_\tau$	Tangential force
$\boldsymbol{F}_{\nabla p}$	Pressure gradient force
$\boldsymbol{F}_{\mathrm{D}}$	Drag force
s_n	Normal overlap
s_τ	Normal overlap
ρ_f	Fluid density
μ_f	Fluid viscosity
$\mathbb{T}_f$	Fluid stress tensor
$\boldsymbol{v}_f$	Fluid velocity Vector
$\overline{\boldsymbol{v}_f}$	Average fluid velocity vector
$\boldsymbol{v}'_f$	Fluctuating fluid velocity vector
α_f	Fluid volume fraction
$\boldsymbol{F}_{p\to f}$	Particle fluid interaction force
τ_{int}	Particle eddy interaction time
τ_e	Eddy lifetime
κ	Turbulent kinetic energy
ε	Turbulent kinetic energy dissipation
τ_r	Time for the particle to transverse the eddy
τ_p	Particle relaxation time
l_e	Eddy characteristic length

open the capsule or individual blister. Subsequently inhaling through the device mouthpiece simultaneously evacuates the dose and carries some fraction of the dose out of the device and into the patient's respiratory tract. For most commercial DPIs, only 15–30% of the drug loaded in a capsule or blister reaches the lungs (Clark et al., 2020).

1.2. DPI resistance considerations

DPIs are often further classified according to their 'resistance', a measure of the inhalation flow rate for a given inhalation effort. Quantitatively, resistance is defined as the slope of a straight line fit through the square root of inspiratory pressure, i.e., the level of pressure generated by the lungs during inhalation, plotted as a function of the corresponding volumetric airflow rate through the device. DPI resistance is classified as low to high depending on the airflow rate achieved at an inspiratory gauge pressure of -4.0 kPa. A DPI is considered to have a low resistance when the airflow rate through it is 90 L/min or greater, a medium resistance when it achieves a flow rate between 60 to 90 L/min, and a high resistance when the flow rate is 60 L/min or less [a device having a flow rate in the 50–60 L/min range may also be referred to as a medium/high resistance DPI]. The resistance of a given DPI is often varied by changing the device inlet size. However, for some DPIs, such inlet size change is often accompanied by some changes in its design (e.g. its shape) as well.

Much of our current understanding of the device resistance and its effect on drug delivery to the lungs is compiled from studies that have compared the lung dose(s) of the various commercial products. However, these commercial products not only had varying device resistances, but also differed in their overall design as well as formulation. Often, studies that attempted to investigate formulation effects underestimated or simply ignored the device contribution (Xu et al., 2010), and vice versa. This approach makes it difficult to truly decouple the effect of device resistance from formulation and device design factors. Nevertheless, the following observations can be drawn from existing literature:

- Increasing the pressure drop across a given device, which is equivalent to increasing the inspiratory pressure (and generally results in an increase in flow rate through the device), for the same formulation typically results in a greater degree of powder dispersion. Here, powder dispersion refers to the deagglomeration of API agglomerates and/or detachments of API particles from the excipient carriers that are typically added to DPI formulations to improve their flowability for capsule or blister filling purposes. This increase in flow rate ultimately leads to increased lung deposition (Clark et al., 2020).
- Increasing the resistance of a given device, which can be achieved by decreasing the size of the device inlet, is anticipated to also improve powder deagglomeration effects as demonstrated by in silico studies performed by Coates et al. (2005a, 2006). These researchers used computational fluid dynamics (CFD) to study how the inlet size of a Cyclohaler®-type DPI affected fine aerosol generation. They showed that smaller inlets (higher resistance) increased the tangential inlet velocity, which then contributed to an increased capsule rotational velocity that ultimately led to improved evacuation of the dose from the capsule. Moreover, the increased resistance was also hypothesized to improve powder deagglomeration as a result of increased shear forces (Coates et al., 2005a; 2006), increased turbulence in the capsule chamber (Coates et al., 2005a), and greater particle impact velocity and frequency.
- From an in vivo perspective, high resistance DPIs are often preferred for the following reasons: (1) they generally result in smaller inspiratory velocity compared to low resistance devices, which increases dose deposition in the peripheral lung region and decreases the inertial effects that could lead to higher oropharyngeal deposition; (2) small variations in inspiratory pressures do not result in significant changes in inspiratory flow, leading to more consistent dosing between patients (Broeders et al., 2003; Hoppentocht et al., 2014; Newman and Busse, 2002); (3) the use of high resistance DPIs have also been associated with greater dilation of the throat and upper airways, which has been found to decrease oropharyngeal dose deposition and increase lung deposition and retention (Svartengren et al., 1996; 1995).

1.3. The use of force control agents in DPI formulations

In recent years, the practice of adding magnesium stearate to DPI formulations has become commonplace. The history of DPI formulations, including the recent transition to dual excipient systems comprised of the API, lactose as a carrier, and magnesium stearate as a ternary excipient, has been summarized by Shur et al. (2016). Generally, it has been shown that the addition of magnesium stearate improves the generation of fine aerosols (Begat et al., 2009; Jetzer et al., 2018; Thalberg et al., 2016). Begat et al. (2009), for example, demonstrated that API that was mechanofused with magnesium stearate achieved significantly more deagglomeration.

In addition, magnesium stearate-bonded API was also less likely to be retained in the DPI. Similar results have been seen from formulations containing lactose (Jetzer et al., 2018) and those containing two or more APIs (Thalberg et al., 2016). The mechanisms driving these trends are hypothesized to involve the reduction of cohesive bonding between API particles, the reduction in carrier excipient 'active' sites–the high energy regions on the surface of the carriers that the API particles tend to attach to Thalberg et al. (2016), as well as lubrication effects. Magnesium stearate's ability to influence the cohesive/adhesive forces between API particles, excipients, and the device surfaces leads to it being referred to as a 'force control agent' (FCA) (Shur et al., 2016). However, while the general effect of magnesium stearate on aerosol performance is well characterized in the literature, how this effect changes when switching from one device resistance to another is currently unclear.

1.4. Numerical modeling to understanding DPI performance

Given the complex interplay between powder formulation and inhaler design, a combination of numerical modeling and experimental assessment to understanding DPI performance has been used in literature. A comprehensive review on the development of the modelling methodologies of flow and particle behaviours in DPI devices can be found in Zheng et al. (2021).

Several papers developed CFD models for DPIs, including the work from Coates et al. (2007, 2005a, 2005b, 2006, 2004), Wong et al. (2010, 2011), Donovan et al. (2012) and Milenkovic et al. (2014). Of particular interest are the studies conducted by Shur et al. (2012, 2015), which emphasized the importance of the interplay between DPI formulation and device resistance. In the former study (Shur et al., 2012), the researchers' goal was to replicate the aerosol performance of the Handihaler device through modified versions of the Cyclohaler®. They found that, while the resistance of the two markedly different devices could be matched by changing the inlet design of the Cyclohaler®, the aerosol characteristics, assessed in vitro through multi-stage cascade impactor experiments, did not match. CFD simulations of air flows inside the two devices suggested that the observed discrepancy was a result of significantly different primary airflow directions in each device, which the authors hypothesized could affect particle/device impacts. In the latter study (Shur et al., 2015), a similar exercise was repeated to achieve comparable (in vitro) performance between a different set of DPIs: the Accuhaler and the Multihaler. The key features of the latter device were again modified in order to match the airflow characteristics of the former device. However, the modified Multihaler® was able to replicate the aerosol characteristics of the Accuhaler® only when the former device was used in combination with a formulation that lowered the API/carrier adhesion. This finding also suggests that CFD analysis alone was not enough to model the complex system.

Using the discrete element method (DEM) (Cundall and Strack, 1979), the interactions between particles, and particles and boundaries are explicitly computed based on established contact models. Coupled CFD-DEM simulations can provide insights that are missing from standalone CFD simulations such as mechanistic understanding of particle-level phenomena like particle interactions, dispersion behavior, and powder deagglomeration. Ultimately, CFD-DEM models can be used to help evaluate how the interplay between the powder, airflow, and device collectively affect the API dispersion and overall DPI performance.

Tong et al. (2010, 2013) and Yang et al. (2008) applied one-way and two-way coupled CFD-DEM methods to investigate the effects of particles/agglomerates size and airflow rate on the power dispersion due to particle-wall collisions in the swirl chamber of the commercial Aerolizer® inhaler. They found that agglomerates formed by smaller particles could only be effectively dispersed at sufficiently high flow velocities. In addition, agglomerates comprised of particles with narrow PSDs were found to be more easily dispersed. Airflow-induced shear was found to be an insignificant factor in agglomerate dispersion. The authors postulated that the dispersion efficiency of DPI inhalers is characterized by the ratio of the impact energy to cohesion energy of the agglomerates.

Recently, Ponzini et al. (2021) analyzed the aerosolization process for a NextHaler® DPI using CFD and CFD-DEM simulations and compared the results against experimental data available in literature. This study highlights the key model parameters that influence the aerosolization process the most such as the selection of CFD boundary conditions, fluid-particle empirical correlations, and DEM contact parameters.

Benque and Khinast (2019) studied the impact of simplifying the capsule motion as having constant rotational speed around a fixed axis by using high-speed image data of capsule motion as an input to the simulations. They showed that capsule-inhaler collisions improved the discharge of a polydisperse model carrier powder from the capsule over a wide range of cohesiveness. Benque and Khinast (2021, 2022) coupled CFD and DEM to model a polydisperse cohesive lactose carrier in an Aerolizer® inhaler considering both constant flow rates and an inhalation profiles of asthmatic children. These studies showed the importance of inhalation profiles and the dependency of the powder discharge rate on the capsule angular position relative to the inhaler air inlets.

1.5. Objectives of the current study

The current study aims to elucidate powder dispersion mechanisms in a capsule-based, single-dose DPI, recognizing its importance in the development of high-dose inhaled therapeutics. Specifically, a combination of in vitro data from cascade impactor measurements of formulations containing high amount of API in blended API-excipients sytems and predictions from a multiphysics model that fully couples CFD and DEM is used to understand factors affecting particle flows in DPIs that in turn affect commonly used fine aerosols metrics: the emitted dose (ED), fine particle dose (FPD), and mean median aerodynamic diameter (MMAD). The separate effects of device resistance, herein evaluated by studying the low and high resistance variants of the Cyclohaler® DPI, and formulation modifications that influence the adhesive bonding between the API/API and API/excipient particles (i.e., the use of force reducing agents) in high-dose formulation systems are investigated, noting that the interplay between these two factors has not been well addressed in the literature and has not been studied via a combination of experimental and numerical approaches previously, particularly for high API loading formulations such as the ones studied herein.

Experimental trends observed from impactor stage depositions and quantities derived from them (namely, the previously mentioned ED, FPD, and MMAD) are correlated with model-predicted parameters that have been shown to be important in determining aerosol performance (see Section 1.4). Factors that influence key aerosol characteristics, e.g., capsule/device dose retention and fine aerosol generation, and how they are affected by differences in the device inlet design and presumed API/excipient adhesion are discussed. The use of model-predicted and experimentally-measured quantities in tandem provides greater insight than using models or experiments separately. Such insight provides new perspectives into formulation-device interactions that, to the best of the authors' knowledge, have never been reported in the literature before.

2. Experimental study of formulation and device resistance effects

2.1. Experimental setup

Two formulations were prepared and tested on the low- and high-resistance RS01 DPI (Plastiape SPA, Osnago LC, Italy). The formulation compositions are summarized in Table 1.

For both formulations, an active pharmaceutical ingredient (API) was micronized using a bench-scale jet-mill (PilotMill-2, Food Pharma Systems, Como, Italy) with the parameters listed in Table 2. For Formulation A, the API was micronized by itself; for Formulation B, a blend of 99.5% w/w API and 0.5% w/w magnesium stearate (Ligamed MF-2-V 'PREMIUM', Peter Greven, Bad Münstereifel, Germany) was co-micronized. The co-micronization process was used as a means to coat the high energy sites on the API particle surfaces with the low surface energy magnesium stearate. Such a method has been hypothesized to reduce the API/excipient adhesion Begat et al. (2004) that ultimately results in a finer particle aerosol.

The API-magnesium stearate blend was prepared by sieving all ingredients using a 250 μm mesh. Approximately 50% of the API was then charged into a stainless steel container, followed by the magnesium stearate, and finally the remaining API portion. The ingredients were then blended together using a Turbula T2F (Willy A Bachofen AG, Muttenz, Switzerland) for 20 min at 45 rpm. The resulting mix was sieved using a 250 μm mesh prior to jet-milling. All processes were performed at 20 °C and 40% RH.

The particle size of both the micronized API and co-micronized API/magnesium stearate mix was measured using laser diffraction analysis (HELOS, Sympatec, Clausthal-Zellerfeld, Germany). A dosing apparatus (ASPIROS, Sympatec, Clausthal-Zellerfeld, Germany) was used to disperse the API during the particle sizing measurement. The particle size data, presented as averages and standard deviations of triplicate measurements, are summarized in Table 3.

Formulations A and B were prepared by blending either the micronized API or the co-micronized API/magnesium stearate mix with inhalation-grade lactose (Lactohale 230, DFE Pharma, Goch, Germany). The preparation began by equilibrating all ingredients at 20 °C/40% RH for 24 hours and then sieving each one through a 250 μm mesh. Next, the lactose was subdivided into approximately four equal parts. The first part was charged into a stainless steel container, followed by either the micronized API or the co-micronized API/magnesium stearate mix, and the second lactose part. These components were subsequently blended together using the Turbula T2F for 20 min at 22 rpm. The resulting intermediate blend was then sieved through a 250 μm mesh. This method was then repeated for mixing the intermediate blend with the remaining lactose parts. All of the previously described steps were performed at 20 °C/40% RH. The final blend was subsequently sieved through a 250 μm mesh, collected in a stainless steel container, and equilibrated for 24 hours at 20 °C/40% RH prior to additional processing.

Blend uniformity was tested by taking ten samples, each weighing

Table 1
Formulation compositions.

Formulation	Composition
A	50.00% w/w API + 50.00% w/w lactose
B	49.75% w/w API + 0.25% magnesium stearate + 50.00% w/w lactose

Table 2
Jet-milling parameters.

Parameters	Setting
Feed rate	0.5 g/min
Grid gauge pressure	2.0 bar
Injection gauge pressure	5.0 bar

Table 3
Particle size distribution characteristics of micronized API and co-micronized API/magnesium stearate.

Material	D10 (μm)	D50 (μm)	D90 (μm)
Micronized API	0.74±0.02	2.10±0.06	4.48±0.04
Co-micronized API/MgSt	0.81±0.05	2.07±0.13	4.06±0.10

10-25 mg, from different locations within the blend. The amount of API in each sample was then assayed against a reference standard via HPLC. The assay mean, %RSD, and acceptance value (AV) for Formulations A and B samples are given in Table 4. As shown, both blends were uniform as per USP < 905 > specifications.

Both formulations were filled into size-3 HPMC capsules using a drum filler (Omnidose TT, Harro Höfliger Verpackungsmaschinen GmbH, Allmersbach, Germany). The working principles of drum fillers and their application to capsule filling of DPI formulations have been described in detail elsewhere (Eskandar et al., 2011; Sibum et al., 2020). Briefly, the core technology of drum fillers is a cylindrical tube (the 'drum') into which small through-bores are precision machined and lined with disposable fine filter paper. During a drum filling process, the formulation is gravity fed onto the drum. A vacuum is then pulled from the center of the drum, causing the powder formulation to be drawn into the bores and form slightly compressed slugs therein. These slugs are subsequently ejected from the bores via compressed air supplied from the center of the tube and collected into capsules. The capsule fill weight is thus dependent largely on the bore volume. For this study, a drum with 25 mm^3 bores was used to achieve a 12 mg fill weight - equivalent to approximately 6 mg of drug in each capsule - for both formulations.

The drug product characteristics relevant to drug delivery into the lungs exhibited by the different combinations of formulations and device resistances were assessed using a Next Generation Impactor (NGI) equipped with a USP induction port ('throat') (Copley Scientific, Nottingham, United Kingdom). The NGI is a type of cascade impactor that is commonly used to quantify the aerodynamic particle size distribution (APSD) of aerosolized drug products. As with any cascade impactor, an aerosolized sample in an NGI passes through a series of stages that become progressively more constrictive toward the outlet. The NGI comprises seven impactor stages and a micro-orifice collector (MOC) that serves as a filter just upstream of the outlet. More detailed descriptions of the NGI, including its USP-standardized specifications, can be found in Marple et al. (2003a,b). As both Formulations A and B contained lactose, a pre-separator was used.

NGI measurements were performed by first affixing a loaded DPI onto the induction port. The capsule was then pierced by using the in-built, spring-loaded, self-retracting needles. The device was subsequently actuated by simulating an inhalation process using a vacuum pump set to achieve a pressure drop of 4 kPa across the inhaler. The air flow rate corresponding to that pressure drop was measured using a volumetric flow meter. The actuation duration was set as the time required to achieve 4 L of air through the device. Following actuation, the API retained in the capsule and the device as well as that deposited in the induction port, pre-separator, and the seven NGI stages were extracted and the corresponding amount was determined by assay against a reference standard through HPLC.

Table 4
Blend content uniformity result for Formulations A and B.

Material	% Mean Assay	% RSD Assay	AV
Formulation A	102.0	2.7	7.0
Formulation B	101.7	5.0	12.4

In addition to the capsule, device, and stage depositions, the following quantities were also determined using the CITDAS software (Copley Scientific Ltd., Nottingham, United Kingdom):

- Emitted dose (ED): the mass of API that makes it out of the device, determined by summing the mass of API deposited in the induction port and subsequent downstream locations.
- Fine particle dose (FPD): the mass of API particles having an aerodynamic diameter less than 5 μm. FPD is determined from the mass of API deposited in stages two through seven of the NGI. It is an estimate of the dose that is expected to be delivered into the lungs.
- Mean median aerodynamic diameter (MMAD): the aerodynamic equivalent diameter below which half of the aerosolized API particle population lies on a mass basis.

2.2. Experimental results

The capsule and device dose retention plus the NGI stage depositions as grouped by device resistance are shown in Fig. 1. The same data sets,

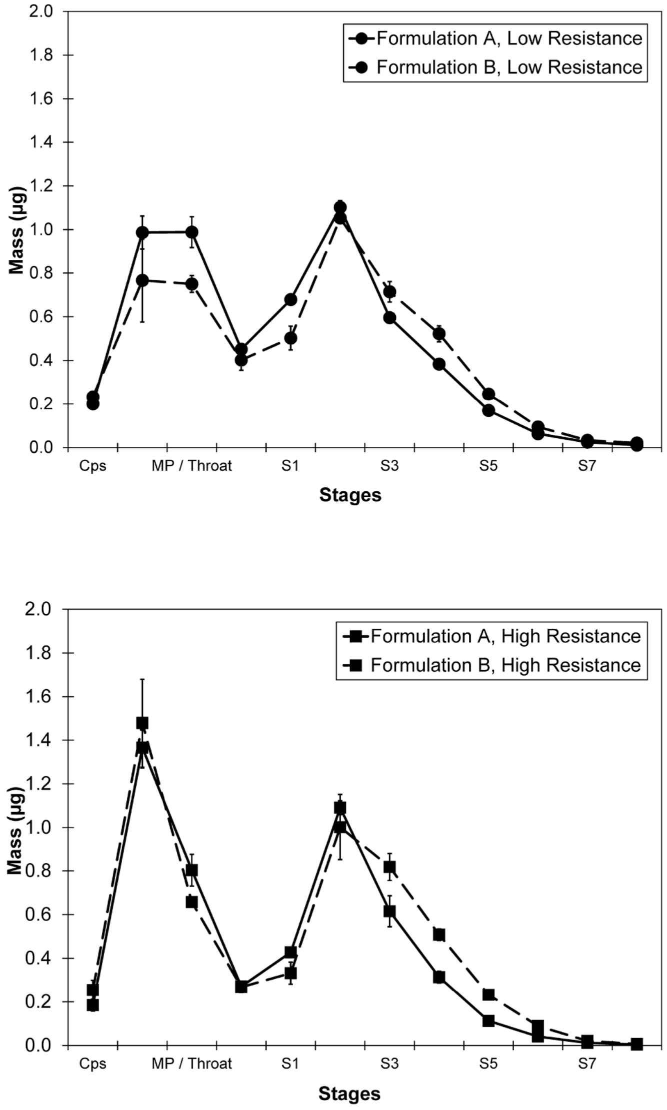

Fig. 1. Dose deposition for low and high resistance inhalers.

but grouped according to the formulation, are presented in Fig. 2. The ED, FPD, and MMAD are summarized in Table 5.

From Fig. 1, it can be seen that ED was not significantly impacted by switching from Formulations A to B. Both the capsule and device depositions are similar. The same trend can be observed from the Table 5 data – for the same device type, changing from Formulation A to Formulation B did not appear to vary the emitted dose. Formulation B universally resulted in a finer aerosol, as evidenced by reduced deposition in the induction port and stage 1 as well as increased deposition in stages 2 through 7 of the NGI. The fine particle dose data in Table 5 show the same trend. This result was likely the contribution of the decreased API/lactose adhesion that resulted from coating the API with the magnesium stearate. The reduction in API/lactose adhesion for Formulation B was further supported by the %RSD data (see Table 4). Here, the larger %RSD and AV for Formulation B, which indicates that that the API in that formulation is less uniformly distributed than in Formulation A, was likely caused by the reduction in API/lactose affinity, again as a result of the magnesium stearate in the blend Begat et al. (2005).

Figure 2 shows that the high resistance inhaler (HRI) retains more particles in the device for both Formulations A and B. Table 5 data shows a larger emitted dose for the low resistance inhaler (LRI) regardless of the formulation. Despite this trend, however, the amount deposited in the induction port, preseparator, and stage 1 of the NGI is also larger for the low resistance device. These results suggest that more large particles exit the low resistance device, indicating that powder dispersion, i.e., deagglomeration of API/API agglomerates and/or the detachments of API from the lactose fillers, likely occurs at a lesser extent. Also, switching from the LRI to the HRI for Formulation A resulted in an increase in the MMAD and a decrease in the fine particle dose (FPD; see Table 5). Interestingly, the opposite trend is observed for Formulation B. In fact, Table 5 MMAD data shows that the finest aerosol was actually generated when using the HRI with Formulation B. Such trends are difficult to explain from the experimental data alone; however, as is demonstrated in the next section, the coupled CFD-DEM model results provide some insights into the factors that may contribute to these results.

Table 5
ED, FPD, and MMAD for Formulations A and B as dispersed from the low and high resistance inhalers.

Material	ED (mg)	FPD (mg)	MMAD (μm)
Formulation A, LRI	4.47±0.12	1.90±0.12	4.13±0.18
Formulation B, LRI	4.34±0.3	2.28±0.05	3.54±0.04
Formulation A, HRI	3.69±0.32	1.34±0.13	4.93±0.06
Formulation B, HRI	3.93±0.12	2.75±0.12	2.77±0.05

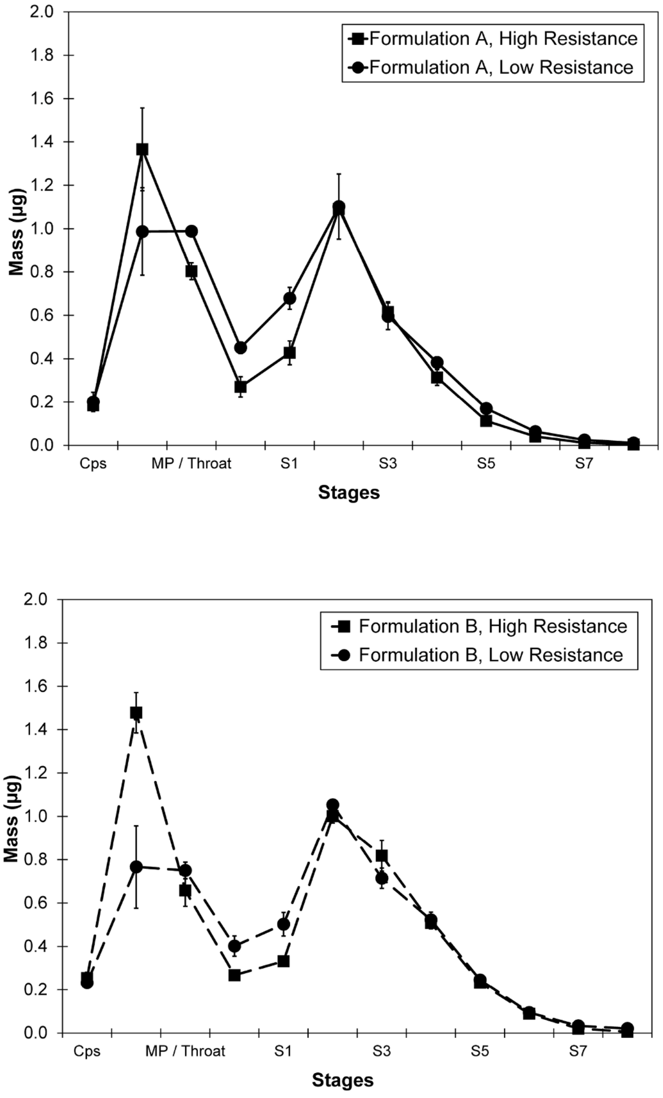

Fig. 2. Dose deposition for Formulations A and B.

3. DEM-CFD model

In the DEM-CFD coupling method, the fluid flow is obtained from a conventional continuum approach using ANSYS Fluent®, in which the conservation equations for mass and momentum are solved by the finite volume method. The solid phase flow is modeled using the discrete approach within Rocky DEM. The coupling between solid and fluid is accomplished by inter-phase momentum terms due to the interaction between phases.

3.1. Numerical scheme

3.1.1. DEM Equations

In DEM, all particles within the computational domain are tracked in a Lagrangian manner by solving explicitly Newton-Euler equations that govern translational and rotational particle motion, respectively:

$$m_p \frac{d\boldsymbol{v}_p}{dt} = \boldsymbol{F}_c + \boldsymbol{F}_{f\to p} + m_p \boldsymbol{g} \tag{1}$$

$$\boldsymbol{J}_p \frac{d\boldsymbol{\omega}_p}{dt} = \boldsymbol{M}_c + \boldsymbol{M}_{f\to p} \tag{2}$$

where m_p is the particle mass, $\boldsymbol{v}_p$ is the particle velocity, $\boldsymbol{g}$ is the gravitational acceleration, $\boldsymbol{\omega}_p$ is the particle angular velocity, $\boldsymbol{F}_c$ is the contact force that accounts for particle-particle and particle-wall interactions, $\boldsymbol{J}_p$ is the particle moment of inertia tensor, and $\boldsymbol{M}_c$ is the net torque generated by tangential forces that causes particle rotation.

Due to the fluid interaction, two additional terms appear when comparing with a pure DEM simulation: $\boldsymbol{F}_{f\to p}$ is the additional force accounting for the interaction with the fluid phase and $\boldsymbol{M}_{f\to p}$ is the additional torque due to the fluid phase velocity gradient.

The contact force, $\boldsymbol{F}_c$, is decomposed into normal and tangential forces. A hysterestic linear spring model (Walton, 1993) was used for the normal contact force, $\boldsymbol{F}_n$. A linear spring Coulomb limit model, an elastic-frictional model (ESSS Rocky, 2022b), is used for the tangential force calculation, $\boldsymbol{F}_\tau$. No adhesive force between particles or between particles and walls was used to model the cohesive behavior of the material.

The pressure gradient, drag, and turbulent dispersion forces were considered as the fluid forces acting on particles. The pressure gradient force, $\boldsymbol{F}_{\nabla p}$, is calculated by:

$$\boldsymbol{F}_{\nabla p} = p\nabla p, \tag{3}$$

where p is the volume of the particle and ∇p is the local pressure gradient.

The drag force acting on the particles, $\boldsymbol{F}_{\mathrm{D}}$, is calculated using the definition of the drag coefficient (Pritchard, 2010), C_D, as:

$$\boldsymbol{F}_{\mathrm{D}} = \frac{1}{2} C_D \rho_f A_p \left| \boldsymbol{v}_f - \boldsymbol{v}_p \right| \left(\boldsymbol{v}_f - \boldsymbol{v}_p \right), \tag{4}$$

where ρ_f is the fluid density, $\boldsymbol{v}_f - \boldsymbol{v}_p$ is the relative velocity between fluid and particle, and A_p is the particle area.

For the drag coefficient calculation, the Huilin-Gidaspow drag correlation (Huilin and Gidaspow, 2003) was chosen as it covers the entire range of solid volume fraction by applying a blending function to promote a smooth transition between the Wen & Yu and Ergun correlations.

The influence of the turbulence over a particle is simulated by means of the interaction with a succession of discrete fluid phase turbulent eddies, similar to the approach described by Gosman and Ioannides (1983). To mimic that a particle is interacting with a turbulent eddy, a random component of velocity is added to the mean fluid velocity provided by the CFD solver. This combined velocity is used to compute the drag acting on the particle during the particle-eddy interaction time, τ_{int}. It is assumed that the turbulence is isotropic and the fluid fluctuating velocity is decomposed as a scalar, $|U|$ and a direction unit vector, $\widehat{\boldsymbol{e}}$:

$$\boldsymbol{v}_f' = |U| \widehat{\boldsymbol{e}}. \tag{5}$$

where $\widehat{\boldsymbol{e}}$ is assumed as a random variable given by a uniform distribution of points over the surface of a unit sphere and $|U|$ is a random variable distributed normally around zero with standard deviation, σ_u, given by:

$$\sigma_u = \sqrt{\frac{2\kappa}{3}}, \tag{6}$$

where κ is the kinetic energy of the turbulence associated with the flow. The eddy lifetime, τ_e, is approximated as:

$$\tau_e = \frac{l_e}{\sigma_u}, \tag{7}$$

where l_e is the characteristic size of the eddy, assumed equal to the dissipation length scale of the system as:

$$l_e = \frac{\sqrt{0.09\kappa^3}}{\varepsilon}, \tag{8}$$

where ε is the dissipation rate of the turbulent kinetic energy associated with the flow.

A further assumption of this turbulence model is that each particle of the simulation has a one-to-one association with a turbulent eddy during an interaction time interval τ_{int}. For estimating this particle-eddy interaction time, two possible outcomes are considered: The particle moves sufficiently slowly relative to the fluid in order to remain within the influence of the eddy during its lifetime, τ_e, or the relative velocity between the particle and the fluid is large enough to allow the particle to transverse the eddy in a transit time, τ_r, shorter than the eddy lifetime. The particle-eddy interaction time is therefore defined as the minimum of the above, i.e.:

$$\tau_{int} = \min(\tau_e, \tau_r). \tag{9}$$

The transit time is estimated from the following solution of a simplified form of the motion equation of a small particle in a fluid medium:

$$\tau_r = -\tau_p \ln\left(1 - \frac{l_e}{\tau_p \left| \boldsymbol{v}_f - \boldsymbol{v}_p \right|}\right). \tag{10}$$

where τ_p is the particle relaxation time defined as:

$$\tau_p = \frac{4\rho_p d_p}{3\rho_f C_D \left| \boldsymbol{v}_f - \boldsymbol{v}_p \right|}. \tag{11}$$

3.1.2. CFD equations

Considering a single-phase flow through a porous medium and assuming that there is no mass transfer between phases, the averaged mass conservation equation of the fluid phase is given by:

$$\frac{\partial}{\partial t}\left(\alpha \rho_f\right) + \nabla \cdot \left(\alpha \rho_f \boldsymbol{v}_f\right) = 0 \tag{12}$$

where the porosity α is defined as the relative volume occupied by the void spaces of the porous region, computed as:

$$\alpha = 1 - \alpha_p \tag{13}$$

where α_p is the local volume fraction of the solid phase at the previous time step, computed by the DEM solver (Ansys, 2021).

Likewise, the averaged momentum equation is:

$$\begin{aligned} &\frac{\partial}{\partial t}\left(\alpha \rho_f \boldsymbol{v}_f\right) + \nabla \cdot \left(\alpha \rho_f \boldsymbol{v}_f \boldsymbol{v}_f\right) = \\ &-\alpha \nabla p + \nabla \cdot \left(\alpha \mathbb{T}_f\right) + \alpha \rho_f \boldsymbol{g} + \boldsymbol{F}_{p \to f} \end{aligned} \tag{14}$$

where p is the pressure, ρ_f is the fluid density, $\boldsymbol{v}_f$ is the fluid phase velocity vector, $\mathbb{T}_f$ is the stress tensor of the fluid phase, and $\boldsymbol{F}_{p \to f}$ is a source term that represents the momentum exchanged between fluid and particles.

The Reynolds-averaged Navier-Stokes (RANS) SST $\kappa - \omega$ turbulence model was used to model the turbulence effects as it provides a good compromise between providing an accurate flow resolution while maintaining a relatively low computational cost by solving only two equations to compute the eddy viscosity. A curvature correction term (Ansys, 2021; Menter, 1994) was added to include the effects of curvature on turbulence as it showed improvements that are competitive with more complex models such as Reynolds Stress Models (RSM) while maintaining the simplicity of eddy viscosity models for curved geometries.

3.1.3. CFD-DEM coupling

In the current DEM-CFD model, the interaction among phases are calculated in a two-step approach:

1. The fluid flow characteristics (physical properties, pressure and velocities fields, etc.) are transferred to the DEM solver and are used to compute the fluid forces acting on particles. These fluid forces are summed with the contact forces acting over the particles to predict their positions and velocities at the next time step. The accumulated values of particle volume and fluid-particle interaction forces per cell are subjected to a mapping procedure before being transferred to the CFD solver as porosity values and momentum source terms. This mapping step transfers the data from the Lagrangian view of the DEM solver into the Eulerian perspective of the CFD solver and also smooths the values to avoid strong fluctuations and non-physical values, which can originate from having many particles with their centroids inside of the same cell.
2. These mapped quantities are transferred to the CFD solver and applied to the solution at the next time step. Local porosity changes will cause fluid to flow into or out of the cell and the momentum sources will bring the influence of the particle motion into the fluid flow in the form of a resistance or a driving force. The fluid flow solution for this subsequent time step, calculated using the information from the DEM solution, will then be transferred to the DEM solver for the computation of the next particle time step. As each solver uses the information from the previous time step of the other solver, they can both work in parallel, using CPU processors for the

fluid phase solution and GPU processing to solve the DEM equations. More details on the coupling between Rocky and Fluent can be found in the CFD coupling manual (ESSS Rocky, 2022a).

3.2. Geometry details and simulation conditions

The computational domain was built according to the geometries of the low and high resistance RS01 device used in the experiments (see Section 2.1). Both devices are a capsule DPI with tangential air inlets that generate swirling airflow to spin the capsule and aerosolize the dose, as shown in Fig. 3. The geometries were modeled with the capsule already pierced and placed inside the spinning chamber, a part of the device in which the capsule is presumed to spin, just below the mouthpiece grid structure (see Fig. 3). The capsule pierced holes are assumed to be circular and 2.0 mm in diameter, and located at the capsule extremities. The molded compartment in which the capsule initially resides just before it is pierced (capsule chamber in Fig. 3) is assumed to be fully sealed (i.e., the needles and any airflow that may enter the device through the needle housing are ignored).

The internal geometries of the low and high resistance devices are largely identical, except for two key differences: the tangential air inlet area of the high resistance device is approximately one-third of the low resistance one and the existence of small ‘pockets’ near the inlets of the high resistance device. These key differences are shown in Fig. 4.

The flow field within the capsule was modeled as the particle-fluid interaction and is the key for correctly capturing the capsule discharge. The CFD domain is composed of two fluid domains: the external one is stationary and contains the chamber with two air inlets, the mouthpiece, and a grid in between whereas the internal domain contains the capsule that rotates around the vertical axis with a fixed, prescribed angular velocity for each of the devices. A sliding mesh model was used for the rotational domain and a mesh interface exists between the two domains as shown in yellow in Fig. 5. The capsule instantaneously rotates at the assigned speed and the spinning velocity, ω, was prescribed as a function of the airflow rate (in liters per minute) in each device, Q, extracted from the work of Coates et al. (2006),

$$\omega\,[RPM] = \begin{cases} 45Q, & \text{for low resistance,} \\ 85Q, & \text{for high resistance.} \end{cases} \tag{15}$$

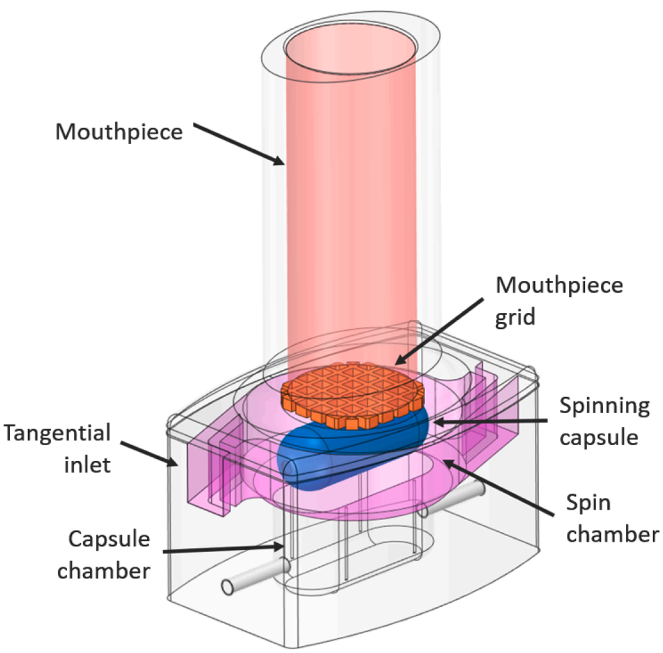

Fig. 3. Drawing of the studied high resistance inhaler including the terminologies for the different parts of the device.

A polyhedral mesh with 1.3×10^6 elements was generated for both cases. A prismatic layer was assigned to the device and capsule walls, as shown in Fig. 6. A pressure inlet condition with a gauge pressure of 0.0 Pa was prescribed at both inlets and an outlet condition with a gauge pressure of -4.0 kPa was prescribed at the outlet. No-slip conditions were prescribed at all walls. Table 6 summarizes the key parameters of the simulation.

Device performance was determined by loading particles with a density of 1500 kg/m^3 inside the capsule and measuring the mass remaining inside the capsule and the domain over time. To minimize computational costs while at the same time assessing the relevant particle size effects on key DPI performance, the simulated particles were distributed in five size groups that encompass the particle size distribution of typical DPI formulations, each with the same number of particles (251,854), as summarized in Table 7. Here, the small particles (3 and 6 μm) are used to represent approximately the median and largest API particles, whereas 12, 24, and 48μm particles were chosen to represent API agglomerates, API particles that adhere to the lactose carriers, and the lactose carriers. The collection of particles amounts to 25 mg of capsule fill weight. While this is different from the experimental capsule fill weight, it is closer to the average fill weights of commercial capsule-based DPI formulations (Newman and Busse, 2002) and thus gives particle quantities that would yield representative fluid-particle interaction in the DPI. Note that the high-dose systems studied here differ significantly from conventional DPI formulations that normally are much lower in drug loading. As the API comprises half the total mass of the formulation, a fraction of the API likely saturates the lactose active sites, leaving a large percentage of the API and API agglomerates in the bulk as free particles, i.e. they likely do not adhere to the lactose carriers. As such, while the API-lactose detachment and API-API deagglomeration were not modeled, the simulated particle statistics are expected to provide a reasonable approximation of the particle population in the system and the corresponding particle dynamics that lead to the particle deagglomeration and detachment events.

3.3. Numerical results

3.3.1. Fluid analyses

The design of the inlet section affects the fluid velocity and turbulence levels generated in the device. Table 8 compiles time-averaged values of the flow data established in the low and high resistance inhalers for the prescribed pressure drop.

For the same pressure drop, the smaller inlet section in the HRI induces greater velocities at the inlet area, generating a higher pressure loss due to friction and reducing the outflow rate established in the device. The model-predicted outflow rates are within 20% of the experimentally-measured counterparts – the NGI flowmeter recorded a value of 60 and 90 L/min for, respectively, the high and low resistance devices. The discrepancy between the experimental and model data is likely caused by slight inaccuracies in the dimensions of the inlet and outlet channels, which were measured manually with a digital caliper. In addition, the casework gap that exists as a result of the two-part device design likely contributes to some leakage. Flow rate measurements performed to compare an as-is high resistance inhaler with one having gaps sealed with putty demonstrated a 12 L/min reduction in flow rate. The former flow rate was measured to be 60 L/min, whereas the latter was 48 L/min. The flow rate of the sealed device is also close to the model-predicted outflow rate (44 L/min). A similar measurement was not performed with the low resistance device as it was assumed that the casework gap did not contribute as much leakage in the low resistance device due to its significantly larger inlets compared to the HRI and the casework gap. In addition, the outflow rates predicted by the coupled CFD-DEM model are also comparable to the results previously published in the literature for similar devices (the Aeroliser®) (Coates et al., 2005a; 2006; Huynh et al., 2015). The outflow rate of 44.4 L/min for the

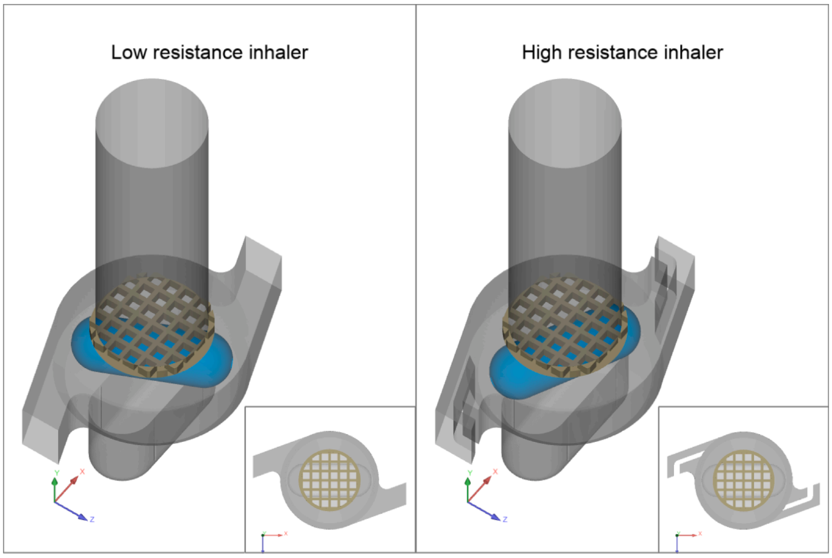

Fig. 4. Comparison of the low and high resistance devices.

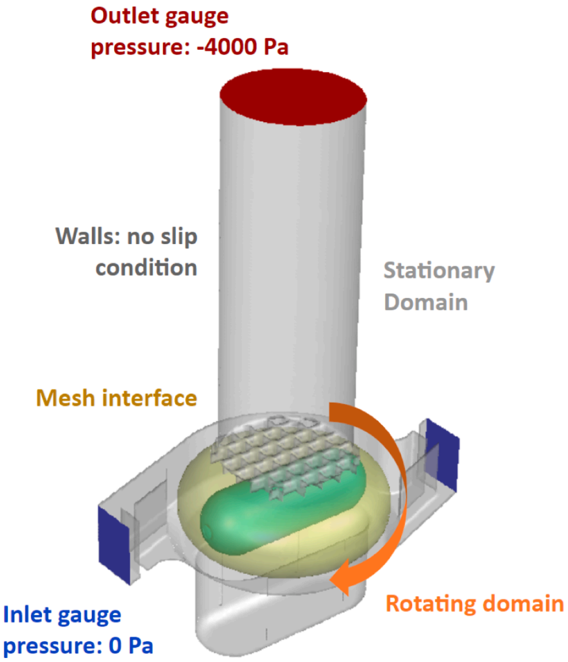

Fig. 5. Schematic view of the inhaler showing CFD boundary conditions.

HRI, for instance, is close to the flow rate of 45.0 L /min, which corresponded to a pressure drop of (4 kPa) and a capsule rotational speed of 3700 rpm), reported in Coates et al. (2006) for a similar device. The mean inhaler resistance for the LRI was found to be 0.019 (kPa$^{1/2}$ /(L.min)), which matches the value reported experimentally by Huynh et al. (2015) for the same device when the capsule is present.

Given that the flow rate is considerably larger in the LRI, the magnitude of the mouthpiece velocity is also larger. Fig. 7 shows the axial velocity in a central vertical plane and in a horizontal plane that crosses the capsule for the LRI (Fig. 7a) and for the HRI (Fig. 7b). As the maximum axial velocity values are located near the grid area, a particle has to move to the central area of the rotating chamber to leave the device. Figure 8 shows the magnitude of the velocity in a plane that intersects the capsule pierced holes and shows that the reduced area causes larger tangential velocities near the inlet region for the HRI, despite the reduced flow rate. The influence of the inlet area on the particle discharge is discussed in Section 3.3.2.

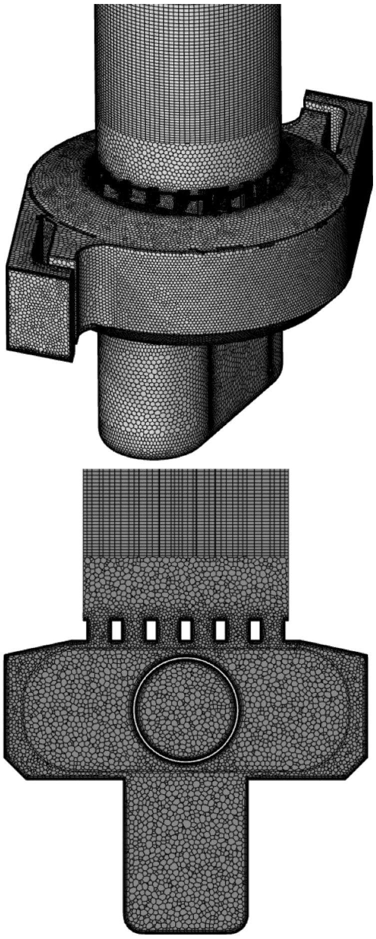

Fig. 6. Details of the polyhedral CFD mesh used in the simulations.

The integral scale strain rate (ISSR), defined as the turbulence eddy dissipation rate divided by the turbulence kinetic energy, is an appropriate parameter to evaluate agglomerate breakup as it gives an estimate of the velocity gradient across the integral scale eddies. Coates et al. (2005a) previously reported that increasing the ISSR and the impact

Table 6
Key parameters of the simulation.

Parameter	Value
Geometrical details	
Capsule length	15.9 mm
Capsule diameter	5.8 mm
DEM parameters	
Particle density	1500 kg/m^3
Particle total mass	25 mg
Capsule rotational speed	Eq. (15)
Particle sliding friction coefficient	0.7
Particle dynamic friction coefficient	0.7
Particle restitution coefficient	0.3
Particle rolling resistance coefficient	0.28
Particle Young's modulus	$1.0 \times 10^7 N/m^2$
DEM time step	1.0×10^{-8} s
CFD parameters	
Mesh elements	1.3×10^6
Air density	1.225 kg/m^3
Air dynamic viscosity	1.789×10^{-5} kg/(m.s)
Inlet gauge pressure	0.0 Pa
Outlet gauge pressure	-4.0 kPa
CFD time step	5.0×10^{-5} s

Table 7
Mass and number of particles in each size group.

Diameter (μm)	Mass (mg)	Number of particles
3	0.00534	251854
6	0.04273	251854
12	0.34181	251854
24	2.73446	251854
48	21.87570	251854

Table 8
Flow and turbulence data.

	Low resistance	High resistance
Capsule velocity (rpm)	4160	3590
Outlet flow rate (L /min)	107.0	47.1
Device resistance ($kPa^{1/2}$ /(L.min))	0.019	0.042
Mouthpiece exit velocity[a] (m /s)	27.0	12.1
Turbulent kinetic energy[b] (J /kg)	12.9	2.8
Integral Scale Strain Rates[b] (1 /s)	12323.5	8718.8

[a] Area averaged. [b] Volume averaged.

velocities in the rotating chamber improved the inhaler dispersion performance up to a critical level, above which the dispersion could not be increased. Figure 9 shows the ISSR values in a central vertical plane and in a horizontal plane that crosses the capsule for the LRI (Fig. 9a) and for the HRI (Fig. 9b). Here, it can be seen that the ISSR in the LRI device is generally larger than that in the HRI one. In addition, larger ISSR values can be observed near the walls and at the grid area, meaning an increased deagglomeration potential for particles that cross this area, for both device types.

3.3.2. Capsule discharge

The in-device swirling airflow provides the necessary momentum to spin the capsule, which in turn provides the centrifugal acceleration that forces powder to exit the capsule. The plot shown in Fig. 10 presents the mass of particles inside the capsule (blue curves) and the capsule discharge rate (red curves) for both the low resistance (solid lines) and high resistance (dashed lines) devices. At the very beginning, the discharge rate increases rapidly as particles leave their initial settled position and move toward the capsule extremities. As the material concentrates near the pierced holes, the capsule mass decreases rapidly and the discharge rate is determined from the balance between the centrifugal force acting on particles and the high-velocity air flow outside the capsule that limits the powder discharge rate. The effect of the airflow through the capsule holes was also described by Benque and Khinast (2019) and highlights the importance of solving the airflow into and out of the capsule in order to capture the capsule discharge behavior. The maximum particle outflow rate is proportional to the rotational velocity, and thus is greater for the low resistance inhaler.

To analyze the influence of the particle size on the capsule discharge, the particle count inside the capsule per particle group was collected as a function of time. The result is shown in Fig. 11. The discharge rate is similar for all groups except for the 3 μm particles, and is slightly larger for the low resistance inhaler as the capsule speed is also larger. It is observed that 3 μm particles are more affected by the recirculating flow within the capsule compared to the other size groups, which causes them to take longer to reach the extremities of the capsule compared to the larger particles, as depicted in Fig. 11. This effect may be explained by observing the results in Fig. 12a which shows the particles colored by their sizes, with increased diameter for visualization purposes, in a thin slice that intersects the capsule, and in Fig. 12b, which shows the fluid velocity vectors at the same locations. Here, it can be seen that API particles and small carrier particles experience significant drag compared to the gravity and centrifugal forces, whereas the larger particles are equally impacted by drag and centrifugal forces. This size effect is also discussed by Benque and Khinast (2019).

In addition, the airflow into the capsule combined with the dome shape of the capsule ends causes a small amount of powder to be retained at the leading side of the pierced holes while it rotates. This retention, however, is significantly smaller compared to the API retention observed experimentally. There are two main reasons for this discrepancy. First, no adhesion force was added to particle-wall interactions even though it is expected that the API has a particularly high Bond number (the ratio of the work of adhesion to the gravitational potential energy). Second, the experimental API has more than 50% of its mass composed of particles smaller than 3.0 μm, as shown in Table 3. For these small particles, the drag effect is more pronounced, causing them to follow the fluid streamlines that circulate within the capsule instead of leaving the capsule. As some of these small particles follow trajectories near the walls, where the fluid velocity is small, there is an increased likelihood that they will adhere to the walls.

To experimentally test the influence of the particle size and particle/capsule adhesion on the capsule retention, capsules were filled with 12 mg of the magnesium stearate-coated API (see Table 1), which is more likely to deagglomerate and thus becomes fluidized in the capsule, and loaded into the devices. The devices were then actuated under the same operating parameters as those used during the NGI tests (see Section 2.1). The API retained in the capsule was then quantified via assay by HPLC. The data are summarized in Table 9, wherein the capsule retentions for both Formulations A and B are also listed. Note that, while the total fill weight was kept the same for the different formulations, the API loading varied. For this reason, the retention amount normalized by the API loading in each formulation is also provided in Table 9.

From Table 9, it can be seen that significantly larger capsule retention resulted when the capsule was filled only with magnesium stearate-coated API. On a nominal basis, the amount of API retained in the capsule filled with only the magnesium stearate-coated API was more than five times that retained in the capsule for Formulations A and B. Table 9 data also show that the capsule retention for Formulations A and B is the same (within experimental uncertainty). These observations suggest that the addition of magnesium stearate in the formulation did not significantly impact capsule retention, likely indicating that the small amount of magnesium stearate coating added to the formulations did not significantly reduce the powder/capsule adhesion or lead to the detachment of the API from the lactose while the particles were still in the capsule. The data also shows that capsule retention was mostly affected by the particle size distribution of the formulation. This observation qualitatively confirms the model trends discussed previously. It also suggests that the coarse lactose particles that the API

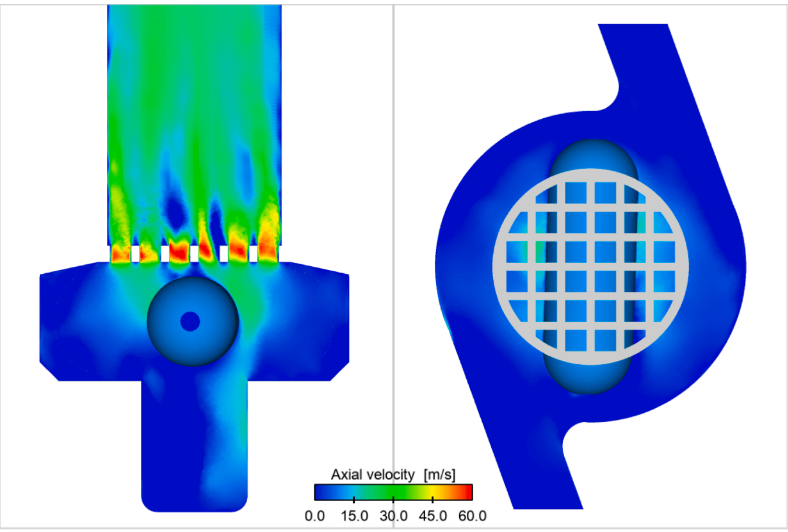

(a) Low resistance inhaler.

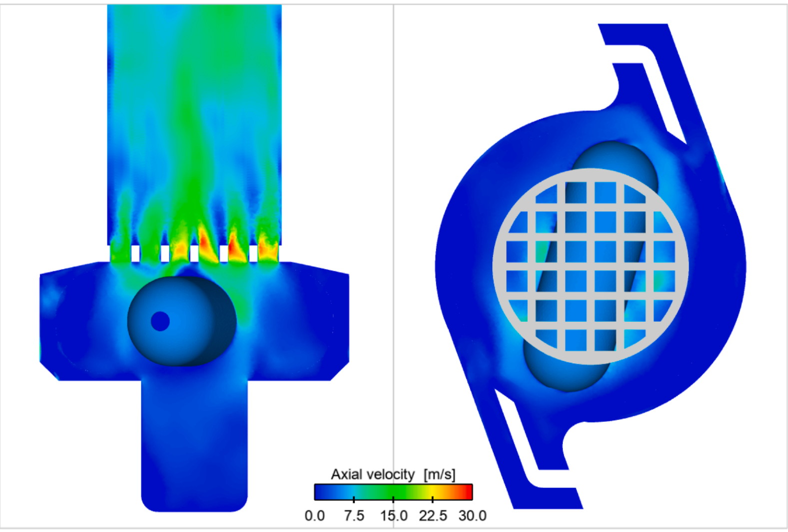

(b) High resistance inhaler.

Fig. 7. Axial fluid velocity in a vertical central plane and a horizontal plane that crosses the capsule. Capsule rotates in the clockwise direction.

particles are blended with and adhere to likely help the powder to disperse out of the capsules.

3.3.3. Device discharge

The effect of the particle size on the device retention can be observed in Fig. 13, which shows the transient number of particles from each size group inside the device, and from Table 10, which shows the percentage of the initial mass of each size group that remained inside the device after 0.8 s. For the LRI, most of the particles smaller than 48 μm are able to leave the device during the simulation period while 24% of the initial mass of particles with size equal to 48 μm is retained in the device.

For the HRI, however, particle retention is considerably larger, particularly for the larger particle sizes. This influence of the inlet design on the particle behavior can be explained by simultaneously examining the particle trajectories together with the fluid velocity field. After leaving the capsule, a particle size segregation effect is observed, as shown in Fig. 14, due to the combination of particle inertia and fluid forces. Small particles move to the center area, where the axial velocity is larger in the spin chamber (as shown in Fig. 7) and are dragged to the mouthpiece section whereas large particles follow trajectories near the walls, where the fluid tangential velocity is larger.

In the low resistance inhaler, however, the high-velocity air that comes from the inlet section pushes particles from this tangential stream to the high axial velocity region of the rotating chamber, causing them to leave the device, as shown in Fig. 14a. The same phenomenon is not observed in the high resistance inhaler as this high-velocity inflow occupies only a narrow annular region close to the walls of the spin chamber and, thus, the inflow does not push large particles towards the center, as shown in Fig. 14b.

It is important to note that in the current simulations, the capsule is set to rotate around a fixed axis. However, in reality, the capsule movement is more random as it also tends to bounce against the device walls. This erratic motion most likely disturbs the air flow and may cause particles to move toward the center of the device, thus reducing the retained dose. This effect was confirmed in the work of Benque and Khinast (2019) which showed improved discharge resulting from capsule-inhaler collisions.

The influence of the pockets on the particle trajectories in the high resistance inhaler was also analyzed. The fluid velocity field near the pocket region is shown in a plane that intersects the capsule in Fig. 15a. All the particles that entered at least once in the pocket region were tagged and Fig. 15b shows the particles that reached velocities smaller than 0.1 m/s while in the pocket region. The plot shown in Fig. 16 compares the number of particles of each size group that entered at least

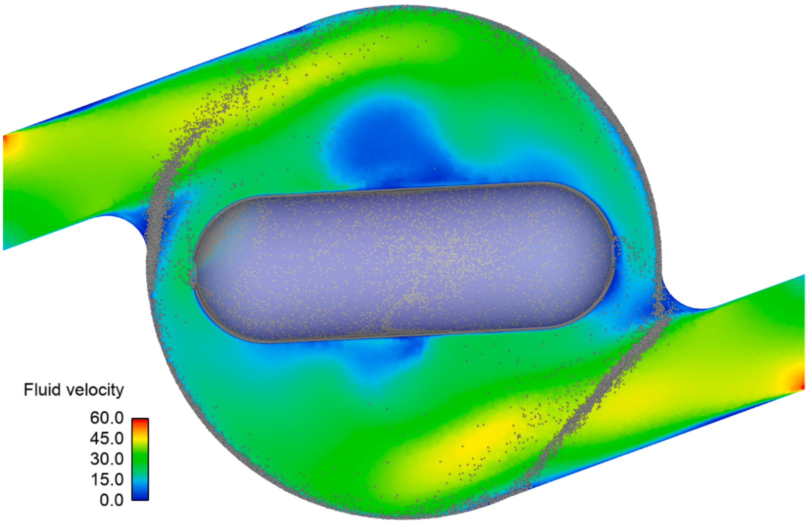

(a) Low resistance inhaler.

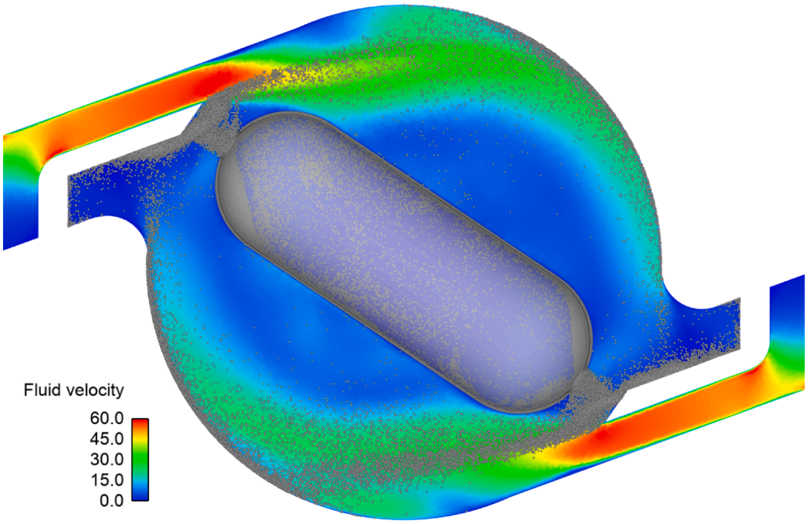

(b) High resistance inhaler.

Fig. 8. Fluid velocity magnitude in a horizontal plane that crosses the capsule (particle rendering size increased for visualization purposes). Capsule rotates in the clockwise direction.

once in the pocket region and the number of these particles that had velocities smaller than 0.1 m/s.

The high fluid tangential velocity causes particles to follow a swirling path near the walls of the capsule chamber. When approaching the pocket region, small particles are able to move inwards toward the center of the spin chamber and continue to follow the fluid swirling path due to their small inertia. That behavior is evidenced by the small number of fine particles that enter the pocket region in Fig. 16. However, large particles, which have greater inertia, tend to impact against the pocket walls and remain in the pocket, as indicated by the number of particles from groups 12, 24, and 48 μm that enter the pocket region. This observation is likely caused by the energy dissipation that results when particles collide against the walls, which when combined with the low fluid velocity in the pocket regions, increases the likelihood of deposition therein. In reality, particle retention in the device pocket is likely even more pronounced as the adhesion force, which is not considered in the simulations, would increase the deposition tendency.

As the DEM method solves all the particle-particle and particle-wall interactions in the system, extensive information about the collisions is available and some statistics can be used for assessing the deagglomeration potential of each device. The impact intensity for each boundary triangle, $I_{b,T}$, is defined as the rate at which work is done on the triangle by the particles and is computed by summing a fraction of work made by the contact forces for all the N_k collisions that occurred during a time interval against each boundary triangle,

$$I_{b,T} = \frac{\sum_{k=1}^{N_k} W_k^b}{A_T \Delta t_{out}}, \tag{16}$$

where A_T is the area of the boundary triangle and Δt_{out} is the data collection time interval. The work W_k^{imp} in a particle-boundary collision is split between particle and boundary according to the ratio of the stiffnesses attributed to the particle, K_p and boundary, K_b,

$$W_k^b = 1 - \frac{K_b}{K_p + K_b} W_k^{imp}, \tag{17}$$

where the impact work, W_k^{imp}, is computed as the summation over the collision duration of the normal force times the overlap. Note that since particle/device adhesion is not modeled in the simulation, particles will bounce off the device walls after impaction and re-enter the fluid stream.

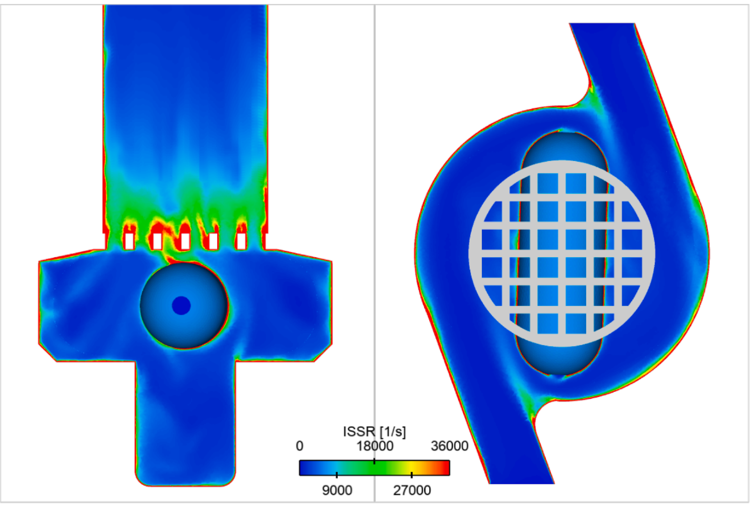

(a) Low resistance inhaler.

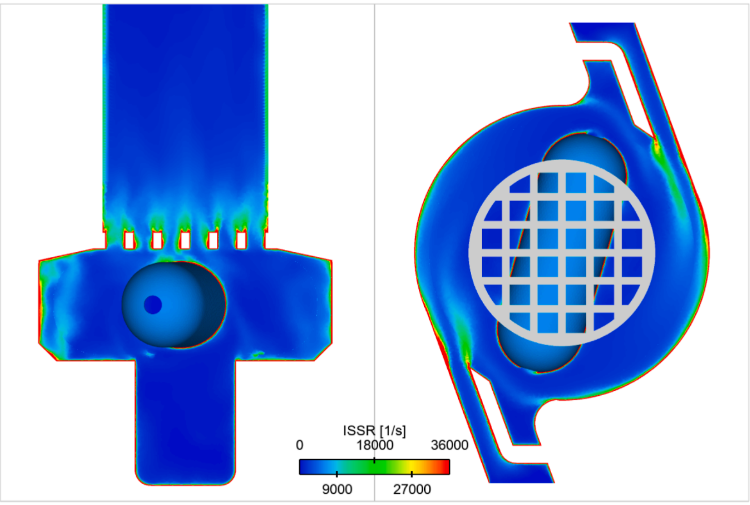

(b) High resistance inhaler.

Fig. 9. Integral scale strain rate (ISSR) in a vertical central plane and a horizontal plane that crosses the capsule. The capsule rotates in the clockwise direction.

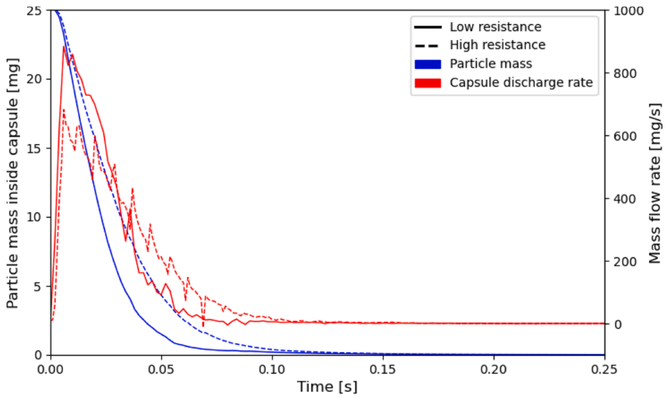

Fig. 10. In-capsule particle statistics: particle mass (blue line) and particle discharge rate (red line) as a function of time for both low (solid line) and high (dashed line) resistance devices. (For interpretation of the references to colour in this figure legend, the reader is referred to the web version of this article.)

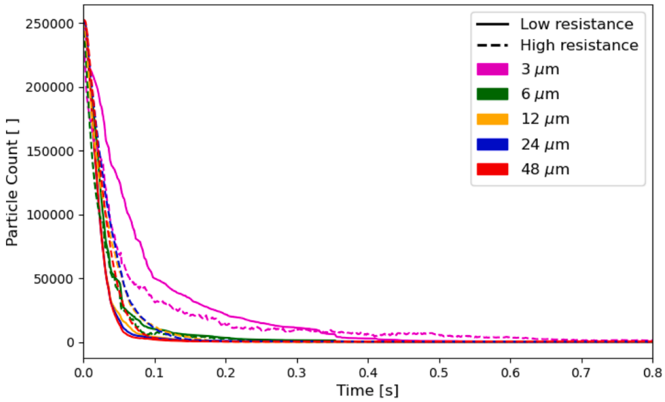

Fig. 11. In-capsule particle count as a function of time, shown for each size group for the low and high resistance devices.

Figure 17 shows the time-averaged impact intensity for the walls of the device. Here, it can be seen that the region with the greatest impact intensity corresponds to the region where the particle stream collides against the wall after being dragged by the fluid with high tangential velocity. Note that, even though the air flow rate is larger for the LRI, the inlet section is narrower for the HRI. As such, the tangential velocities are also larger for the HRI (see Fig. 8). Accordingly, particles reach higher velocities within this section of the HRI device, resulting in higher impact work when they collide against walls.

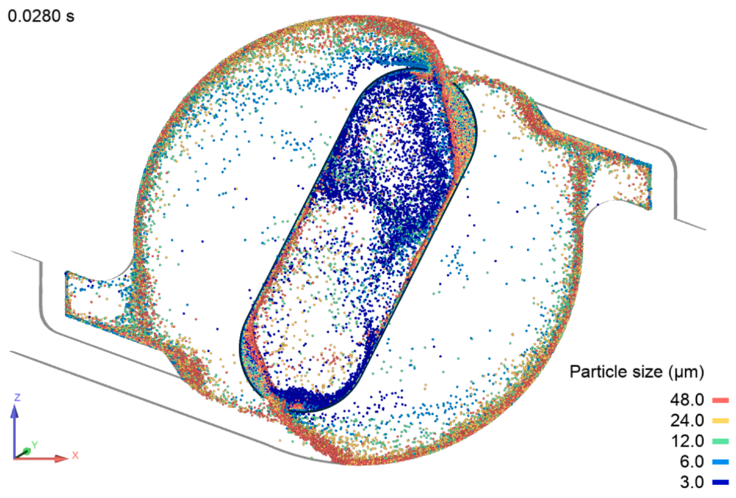

(a) Particles in a plane that cuts the capsule (particles shown as same size spheres - size given by the size scale).

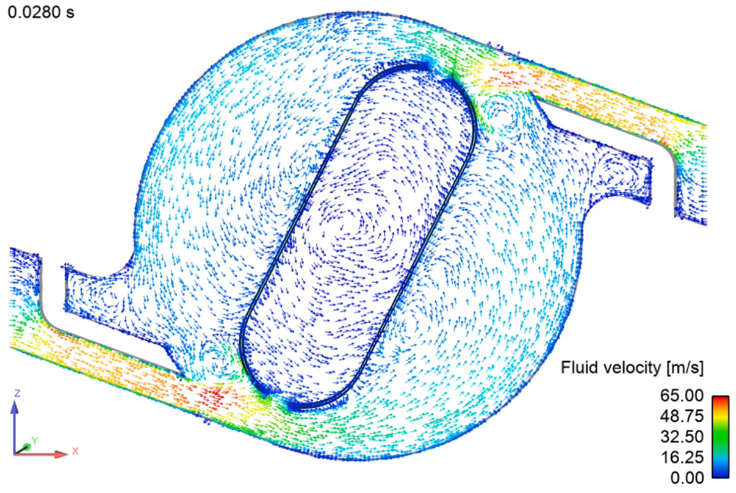

(b) Flow vectors in a plane that cuts the capsule (magnitude given by the color scale).

Fig. 12. Particle flow inside capsule. Capsule rotates in the counter-clockwise direction.

Table 9
Capsule retention for different formulations. Data shown are averages and standard deviations of triplicate experimental measurements.

	Nominal (mg)	%-Loaded Dose (%)[a]
Mg Stearate-Coated API, LRI	1.22±0.04	10.21±0.37
Mg Stearate-Coated API, HRI	1.20±0.12	10.09±1.01
Formulation A, LRI	0.20±0.02	3.34±0.40
Formulation A, HRI	0.18±0.05	3.08±0.75
Formulation B, LRI	0.23±0.01	3.90±0.19
Formulation B, HRI	0.25±0.03	4.26±0.45

[a] Nominal dose retention divided by loaded dose (=12 mg for the mg stearate-coated API formulation and 6 mg for Formulations A and B).

4. Discussion: Factors critical to ED, FPD, and MMAD

From the preceding discussions, factors important for powder dynamics in the capsule and the device are summarized as follows:

i Capsule discharge is driven by two opposing forces: the centrifugal acceleration that pushes the powder towards the pierced holes and the airflow into the capsule that prohibits powder from discharging from the capsule. The latter factor is predicted to affect small (< 3 μm) particles more than large ones. Model data (see Fig. 11) shows similar capsule discharge trends between the low and high resistance

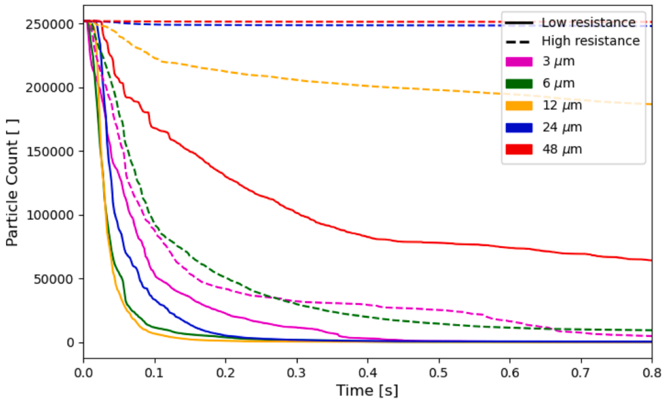

Fig. 13. Predicted device discharge per particle size group.

Table 10
Predicted mass retention inside the device after 0.8 s.

	Low resistance (%)	High resistance (%)
3 μm	0.016	0.968
6 μm	0.002	2.425
12 μm	0.011	68.648
24 μm	0.077	97.981
48 μm	24.740	99.039
Device retention	21.657	98.321

devices. Both results are corroborated with experimental observations (see Table 9).

ii The effect of inlet size is complex and is likely confounded by the different flow rates between the low and high resistance devices for the same outlet pressure. For the LRI, the flow field resulting from the inlet inflow is such that a wide range of particle size classes are more likely to be dragged towards the axial flow that transports them out of the device. The inlet inflow of the HRI, on the other hand, generates an effect akin to a cyclonic separator, wherein large particles are confined to move within the tangential flow field close to the walls of the capsule spin chamber (i.e., the part of the device where the capsule spins) due to their inertia, whereas small particles are able to be entrained by the axial flow that drags them toward the mouthpiece. Due to the higher flow rate of the LRI, more momentum is also available to move larger particles out of the device.

iii The highly turbulent flow field just downstream of the device grid structure (shown in Fig. 9) likely serves as a means for breaking up API agglomerates and/or detaching API particles from the excipient carriers. Since the grid structure and mouthpiece dimensions are identical for both the LRI and HRI, the higher flowrate LRI generates higher ISSR in that region. The LRI therefore likely provides more dispersive capacity for the powder that passes through the grid structure compared to the HRI.

iv Particle/device impaction along the walls of the capsule spin chamber that can lead to powder deagglomeration is predicted to occur to a greater extent for the HRI. This behavior is a direct result of the faster moving tangential flow in the HRI case.

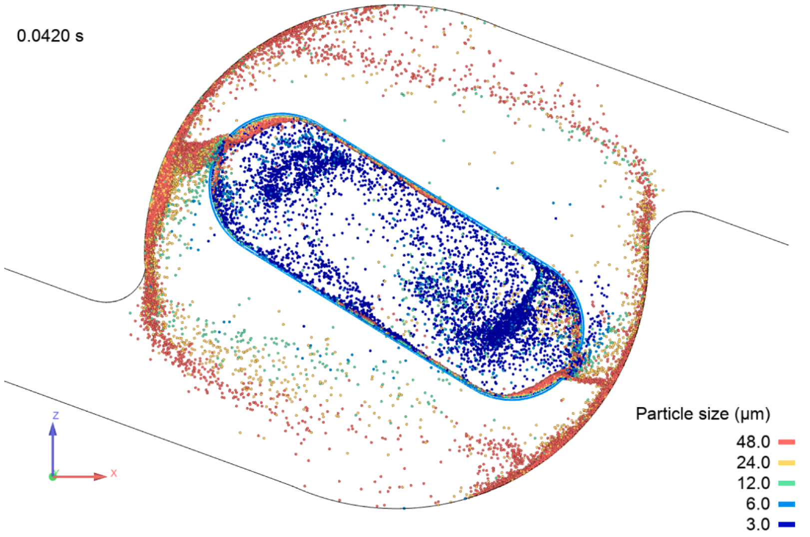

(a) Particle flow in a section of the LRI device. Particles are colored by size, with the size increased for visualization purposes.

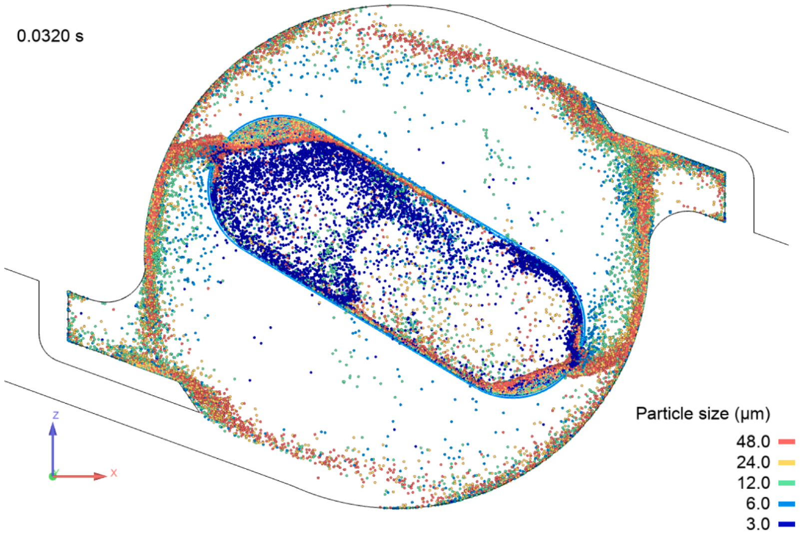

(b) Particle flow in a section of the HRI device. Particles are colored by size, with the size increased for visualization purposes.

Fig. 14. Particle flow inside capsule. Capsule rotates in the counter-clockwise direction.

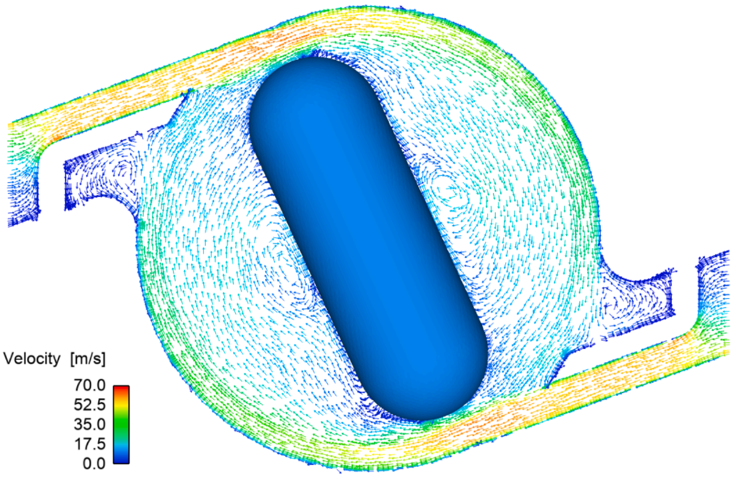

(a) Fluid velocity vectors in a plane that intersects the capsule, colored by the fluid velocity magnitude. Capsule rotates in the clockwise direction.

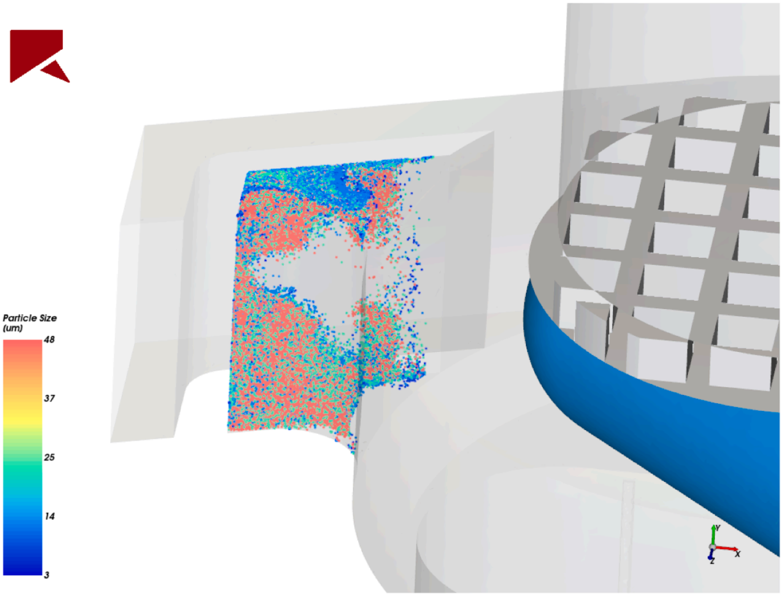

(b) Particles that entered the pocket region and had velocities smaller than $0.1\ \mathrm{m\,s^{-1}}$ (particle rendering size increased for visualization purposes, colored by their sizes).

Fig. 15. Fluid velocity field and particle with small velocities in the pocket region.

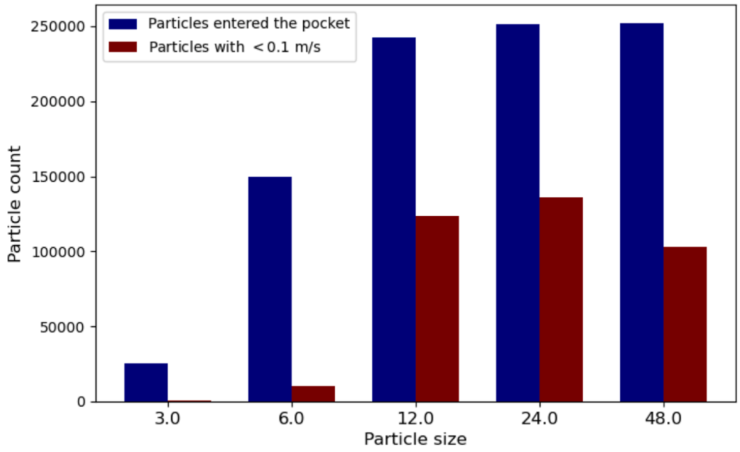

Fig. 16. Number of particles per size group that entered the pocket region and number of particles with velocity smaller than 0.1 ms^{-1} that entered the pocket region.

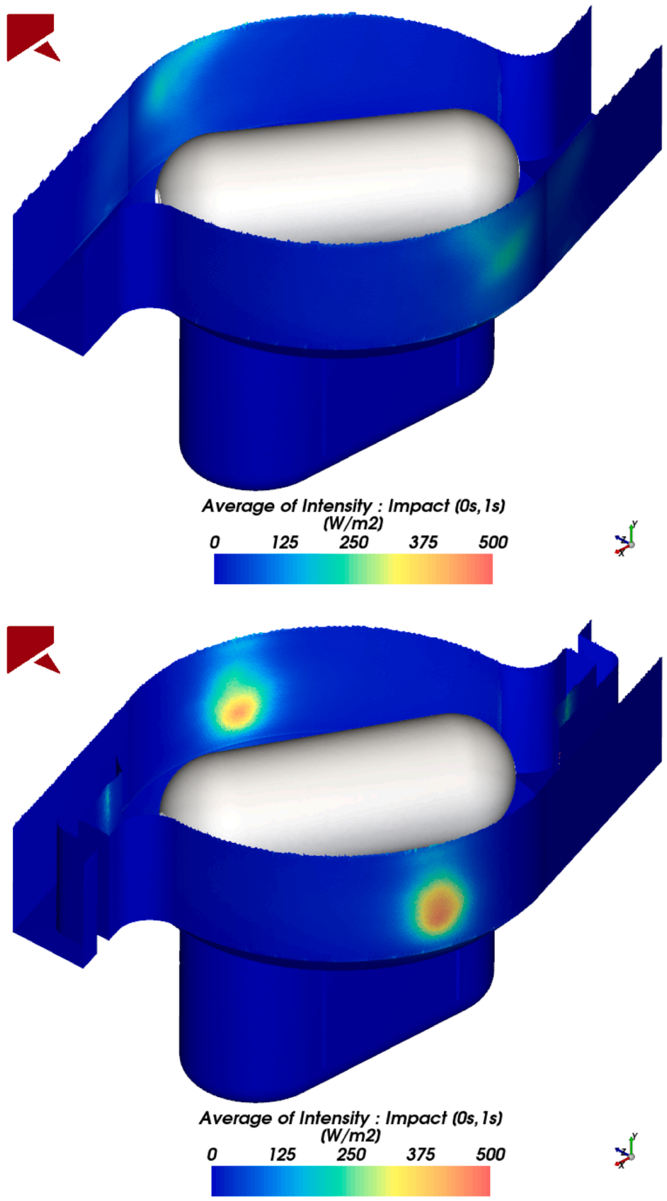

Fig. 17. Time averaged impact intensity for the low and high resistance inhalers.

v Small pockets near the inlet of the high resistance device likely contribute to increased particle deposition therein. In addition, the predicted fluid/particle dynamics also show that larger particles are more likely to be deposited in these pockets.

In the context of the experimental observations, the following are hypothesized – first, both (ii) and (v) would make the HRI more likely to retain more particles compared to the LRI. This prediction is consistent with the emitted dose data in Table 5. Furthermore, in the case where Formulation A, which is expected to have greater API/lactose adhesion and API/API cohesion than Formulation B, is paired with the high resistance device, the deagglomeration effect described in (iv) is likely insufficient to break apart API agglomerates and disperse a large portion of the API from the coarser lactose particles. As a result of (ii), these API particles then tend to remain in the device together with the lactose, causing this formulation/device combination to have the least ED.

Switching from HRI to LRI for the same formulation causes more coarse particles to be dragged to the mouthpiece section due to the mechanisms described in (ii). In turn, this behavior results in an increase in ED, which is consistent with Table 5 data. In addition, since the low resistance device also generates higher ISSR around the grid structure (see (iii) above), the portion of the emitted dose that is comprised of fine particles is likely greater for the LRI than for the HRI. This prediction is also consistent with Table 5 data – the fine particle fractions, which can be evaluated by dividing the fine particle dose by the emitted dose, for Formulation A/HRI and Formulation A/LRI combinations are, respectively, 36.3% and 46.5%. Table 5 data also shows a reduction in MMAD when switching from HRI to LRI for Formulation A, suggesting that a finer aerosol is generated as a result of this device switch.

Switching from Formulation A to B while using the low resistance device likely leads to an increase in fine particle generation. This result occurs because the dispersive effect outlined in (iii) likely occurs to a greater extent when there is less API/lactose adhesion and API/API cohesion. This trend is also reflected by an increase in FPD and a decrease in MMAD in Table 5. Additionally, the fine particle fraction for the Formulation B/LRI combination (= 53.5%) is also larger than that for the Formulation A/LRI combination. Moreover, since the size distribution of the coarser portions of Formulations A and B is the same, the impact of (i) and (ii) on both the capsule and device discharge is largely the same for either formulation. As a result, the emitted dose would tend to remain unchanged following a formulation switch if the device is kept the same. This behavior is in agreement with Table 5 data.

Switching from LRI to HRI for Formulation B would likely generate an even finer aerosol. This behavior is due to the combined effects of (iii) and (iv), both of which are amplified when there is less adhesion between the API and the lactose and less cohesion between the API particles. Table 5 data corroborates this expectation: the fine particle dose of the Formulation B/HRI combination is the highest compared to the other formulation/device combinations and its MMAD is the smallest. Lastly, its fine particle fraction is also the highest (= 70.0%).

For the formulations studied in the current work, powder deagglomeration is likely achieved primarily by overcoming the API/API cohesion and API/lactose adhesion. In such a system, both model and experimental data suggest that the high resistance device provides better dispersing capacity, owing to the particle/device impaction that occurs to a greater extent therein, than the low resistance device when formulations that are similar to Formulation B are used. For more adhesive formulations, however, the low resistance device is likely the better option as its larger inlets and higher flow rate provide it with greater capacities to lift more particles toward the mouthpiece and generate a more intense turbulent field around the grid structure, which in turn increases the likelihood of fine particle generation than the high resistance device. These results also reinforce the importance of studying DPI formulations in combination with the device of choice as there is no universal optimal formulation or universal optimal device; there is only an optimal device-formulation combination.

Model results also provide several means to improve the performance of the HRI. For example, the HRI pockets can be eliminated so particles do not accumulate there. In addition, the capsule spin chamber design can also be slightly modified–the device wall section where the highest impact energy is observed in Fig. 17 can be made flat and more normal to the direction of the air inflow to maximize the particle deagglomeration effects discussed previously.

5. Conclusions

The discussions presented herein highlight the complex fluid and particle dynamics that result from formulation and device design features and the interplay between the two. The coupled CFD-DEM model described in the current study was found to be capable of capturing some of these complex physics, providing valuable insights into the device performance by capturing the in-device fluid dynamics and particle interactions that, in turn, provide a mechanistic understanding of key experimental trends. In addition, factors that drive the powder discharge process from the capsule and ultimately the device, as well as those that are hypothesized to affect the aerosol properties, can likely only be captured accurately when considering a multiphysics approach. The complex fluid/particle interactions that are present in the spin chamber, for instance, are likely impossible to be described if using only a standalone CFD or a standalone DEM model.

For the RS01 systems studied in the current work, the fully coupled simulation shows that by simply changing the device inlet size, the primary mechanisms by which powder deagglomeration occurs also changes. For the device with a smaller inlet (high resistance), powder dispersion occurs as a result of particle/device impaction, and to a lesser extent, the turbulent field generated just downstream of the device grid structure. The particle/device impaction of the larger inlet device (low resistance) is predicted to be four times less intense than that of the high resistance device. For this device variant, then, the dispersive capacity likely comes largely from its ability to move a wider range of particle size classes and utilizing the turbulent field generated near the grid to disperse them. These differing deagglomeration mechanisms subsequently affect different formulations differently. By correlating model results to experimental trends we hypothesize that formulations that include a force control agent that potentially reduces the cohesive bond between API particles and adhesive bond between the API fines and the excipient carriers can likely generate finer aerosols if paired with the high resistance device variant, whereas more cohesive formulations are likely more compatible with the low resistance variant.

While the current model includes some simplifying assumptions and considers only idealized particles and, thus, cannot provide more quantitative predictions, improvements can likely be made by properly calibrating the model against experimental data, which can be achieved by simulating more realistic particle shapes and including API/API cohesion, API/excipient adhesion, and particle/device adhesion. In addition, more accurate physics can also be incorporated. As an example, the capsule motion in the device can be predicted as part of the DEM solutions. In addition, the large eddy simulation (LES) turbulence model can be used in place of the RANS-based model incorporated in the current study to more accurately describe the turbulence anisotropies that can potentially impact the particle dynamics in the capsule, thus affecting the particle discharge therefrom, as well as those near the grid area, where API/API deagglomeration and API/excipient detachment are expected to occur. Further, a time-dependent pressure profile matching that prescribed for the NGI test can be assigned as the inlet boundary condition in the CFD model. Such transient profile may impact the flow field and capsule motion (if it is predicted from the simulation), which subsequently affects the particle evacuation process from the capsule and the device. One potential application of a well-calibrated coupled model is to aid in device design optimization for a given formulation to maximize both emitted dose and fine aerosol generation while reducing, if not eliminating, the prototype cycle.

CRediT authorship contribution statement

Lucilla C. Almeida: Conceptualization, Methodology, Validation, Software, Writing – original draft, Writing – review & editing, Visualization. **Rahul Bharadwaj:** Conceptualization, Supervision. **Avi Eliahu:** Investigation, Writing – review & editing, Validation, Resources, Supervision. **Carl R. Wassgren:** Supervision, Writing – review & editing. **Karthik Nagapudi:** Investigation, Writing – review & editing. **Ariel R. Muliadi:** Conceptualization, Methodology, Validation, Writing – original draft, Writing – review & editing, Visualization, Project administration.

Declaration of Competing Interest

The authors declare that they have no known competing financial interests or personal relationships that could have appeared to influence the work reported in this paper.

Acknowledgments

The authors would like to thank Vinicius Daroz (ESSS) and Jerry Tso (Genentech) for providing valuable inputs and for being a reliable source of information for this study; Stuart Abercrombie (Team Consulting) for his work on the device characterizations and leak testing; and Nanopharm/Aptar for preparing the formulation and performing the NGI characterizations for this study.

References

Ansys, 2021. Fluent® Theory Guide, Release 2021 R2. ANSYS, Inc.

Begat, P., Morton, D.A., Shur, J., Kippax, P., Staniforth, J.N., Price, R., 2009. The role of force control agents in high-dose dry powder inhaler formulations. J. Pharm. Sci. 98 (8), 2770–2783.

Begat, P., Morton, D.A., Staniforth, J.N., Price, R., 2004. The cohesive-adhesive balances in dry powder inhaler formulations I: direct quantification by atomic force microscopy. Pharm. Res. 21, 1591–1597.

Begat, P., Price, R., Harris, H., Morton, D.A., Staniforth, J.N., 2005. The influence of force control agents on the cohesive-adhesive balance in dry powder inhaler formulations. KONA Powder Part. J. 23, 109–121.

Benque, B., Khinast, J.G., 2019. Understanding the motion of hard-shell capsules in dry powder inhalers. Int. J. Pharm. 567, 118481.

Benque, B., Khinast, J.G., 2021. Estimating inter-patient variability of dispersion in dry powder inhalers using CFD-DEM simulations. Eur. J. Pharm. Sci. 156, 105574.

Benque, B., Khinast, J.G., 2022. Carrier particle emission and dispersion in transient CFD-DEM simulations of a capsule-based DPI. Eur. J. Pharm. Sci. 168, 106073.

Broeders, M., Molema, J., Hop, W., Folgering, H., 2003. Inhalation profiles in asthmatics and COPD patients: reproducibility and effect of instruction. J. Aerosol. Med. 16, 131–141.

Clark, A.R., Weers, J.G., Dhand, R., 2020. The confusing world of dry powder inhalers: it is all about inspiratory pressures, not inspiratory flow rates. J. Aerosol Med. Pulm. Drug Deliv. 33 (1), 1–11.

Coates, M.S., Chan, H.-K., Fletcher, D.F., Chiou, H., 2007. Influence of mouthpiece geometry on the aerosol delivery performance of a dry powder inhaler. Pharm. Res. 24 (8), 1450–1456.

Coates, M.S., Chan, H.-K., Fletcher, D.F., Raper, J.A., 2005. Influence of air flow on the performance of a dry powder inhaler using computational and experimental analyses. Pharm. Res. 22 (9), 1445–1453.

Coates, M.S., Fletcher, D.F., Chan, H.-K., Raper, J.A., 2005. The role of capsule on the performance of a dry powder inhaler using computational and experimental analyses. Pharm. Res. 22 (6), 923–932.

Coates, M.S., Chan, H.-K., Fletcher, D.F., Raper, J.A., 2006. Effect of design on the performance of a dry powder inhaler using computational fluid dynamics. Part 2: air inlet size. J. Pharm. Sci. 95 (6), 1382–1392.

Coates, M.S., Fletcher, D.F., Chan, H.-K., Raper, J.A., 2004. Effect of design on the performance of a dry powder inhaler using computational fluid dynamics. Part 1: grid structure and mouthpiece length. J. Pharm. Sci. 93 (11), 2863–2876.

Cundall, P.A., Strack, O.D.L., 1979. A discrete numerical model for granular assemblies. Geotechnique 29, 47–65.

de Boer, A.H., Hagedoorn, P., Hoppentocht, M., Buttini, F., Grasmeijer, F., Frijlink, H.W., 2017. Dry powder inhalation: past, present and future. Expert Opin. Drug Deliv. 14 (4), 499–512.

Donovan, M.J., Kim, S.H., Raman, V., Smyth, H.D., 2012. Dry powder inhaler device influence on carrier particle performance. J. Pharm. Sci. 101 (3), 1097–1107.

Eskandar, F., Lejeune, M., Edge, S., 2011. Low powder mass filling of dry powder inhalation formulations. Drug Dev Ind Pharm 37 (1), 24–32.

ESSS Rocky, 2022. CFD Coupling Technical Manual. Release 2022 R1. ESSS Rocky DEM, S.R.L.

ESSS Rocky, 2022. DEM Technical Manual. Release 2022 R1. ESSS Rocky DEM, S.R.L.

Gosman, A.D., Ioannides, E., 1983. Aspects of computer simulation of liquid-fueled combustors. J. Energy 7, 482–490.

Hoppentocht, M., Hagedoorn, P., Frijlink, H., de Boer, A., 2014. Technological and practical challenges of dry powder inhalers and formulations. Adv. Drug Deliv. Rev. 75.

Huilin, L., Gidaspow, D., 2003. Hydrodynamics of binary fluidization in a riser: CFD simulation using two granular temperatures. Chem. Eng. Sci. 58, 3777–3792.

Huynh, B.K., Chen, Y., Fletcher, D.F., Young, P., Zhu, B., Traini, D., 2015. An investigation into the powder release behavior from capsule-based dry powder inhalers. Aerosol Sci. Technol. 49 (10), 902–911.

Jetzer, M.W., Morrical, B.D., Schneider, M., Edge, S., Imanidis, G., 2018. Probing the particulate microstructure of the aerodynamic particle size distribution of dry powder inhaler combination products. Int. J. Pharm. 538 (1–2), 30–39.

Marple, V.A., Olsson, B., Santhanakrishnan, K., Mitchell, J.P., Murray, S.C., Hudson-Curtis, B.L., 2003. Next generation pharmaceutical impactor (a new impactor for pharmaceutical inhaler testing). part ii: archival calibration. J. Aerosol Med. 16 (3), 301–324.

Marple, V.A., Roberts, D.L., Romay, F.J., Miller, N.C., Truman, K.G., Oort, M.V., Olsson, B., Holroyd, M.J., Mitchell, J.P., Hochrainer, D., 2003. Next generation pharmaceutical impactor (a new impactor for pharmaceutical inhaler testing). Part I: design. J. Aerosol Med. 16 (3), 283–299.

Menter, F., 1994. Two-equation eddy-viscosity turbulence models for engineering applications. AIAA J. 32, 1598–1605.

Milenkovic, J., Alexopoulos, A., Kiparissides, C., 2014. Deposition and fine particle production during dynamic flow in a dry powder inhaler: a CFD approach. Int. J. Pharm. 461 (1), 129–136.

Newman, S., Busse, W., 2002. Evolution of dry powder inhaler design, formulation, and performance. Respir. Med. 96 (5), 293–304.

Ponzini, R., Da Viá, R., Bná, S., Cottini, C., Benassi, A., 2021. Coupled CFD-DEM model for dry powder inhalers simulation: validation and sensitivity analysis for the main model parameters. Powder Technol.

Pritchard, P.J., 2010. Fox and McDonald's Introduction to Fluid Mechanics, 8th ed. John Wiley & Sons.

Shur, J., Lee, S., Adams, W., Lionberger, R., Tibbatts, J., Price, R., 2012. Effect of device design on the in vitro performance and comparability for capsule-based dry powder inhalers. AAPS J. 14 (4), 667–676.

Shur, J., Price, R., Lewis, D., Young, P.M., Woollam, G., Singh, D., Edge, S., 2016. From single excipients to dual excipient platforms in dry powder inhaler products. Int. J. Pharm. 514 (2), 374–383.

Shur, J., Saluja, B., Lee, S., Tibbatts, J., Price, R., 2015. Effect of device design and formulation on the in vitro comparability for multi-unit dose dry powder inhalers. AAPS J. 17 (5), 1105–1116.

Sibum, I., Hagedoorn, P., Botterman, C.O., Frijlink, H.W., Grasmeijer, F., 2020. Automated filling equipment allows increase in the maximum dose to be filled in the cyclops® high dose dry powder inhalation device while maintaining dispersibility. Pharmaceutics 12 (7), 645–659.

Staquicini, D.I., Barbu, E.M., Zemans, R.L., Dray, B.K., Staquicini, F.I., Dogra, P., Cardó-Vila, M., Miranti, C.K., Baze, W.B., Villa, L.L., Kalil, J., Sharma, G., Prossnitz, E.R., Wang, Z., Cristini, V., Sidman, R.L., Berman, A.R., Panettieri, R.A., Tuder, R.M., Pasqualini, R., Arap, W., 2021. Targeted phage display-based pulmonary vaccination in mice and non-human primates. Med 2 (3), 321–342.e8.

Svartengren, K., Anderson, M., Svartengren, M., Philipson, K., Camner, P., 1996. Oropharyngeal deposition of 3.5 μm particles inhaled through an elongated mouthpiece. Eur. Respir. J. 9, 1556–1559.

Svartengren, P.K., Lindestad, P., Svartengren, M., Philipson, Bylin, G., Camner, P., 1995. Added external resistance reduces oropharyngeal deposition and increases lung deposition of aerosol particles in asthmatics. Am. J. Respir. Crit. Care Med. 152, 32–37.

Thalberg, K., Åslund, S., Skogevall, M., Andersson, P., 2016. Dispersibility of lactose fines as compared to API in dry powders for inhalation. Int. J. Pharm. 504 (1–2), 27–38.

Tong, Z., Yang, R., Chu, K., Yu, A., Adi, S., Chan, H., 2010. Numerical study of the effects of particle size and polydispersity on the agglomerate dispersion in a cyclonic flow. Chem. Eng. J. 164 (2), 432–441.

Tong, Z., Zheng, B., Yang, R., Yu, A., Chan, H., 2013. CFD-DEM investigation of the dispersion mechanisms in commercial dry powder inhalers. Powder Technol. 240, 19–24.

Walton, O., 1993. Numerical Simulation of Inelastic, Frictional Particle-Particle Interactions. In: Butterworth-Heinemann Series in Chemical Engineering. Butterworth-Heinemann.

Wong, W., Fletcher, D.F., Traini, D., Chan, H.-K., Crapper, J., Young, P.M., 2010. Particle aerosolisation and break-up in dry powder inhalers 1: evaluation and modelling of venturi effects for agglomerated systems. Pharm. Res. 27 (7), 1367–1376.

Wong, W., Fletcher, D.F., Traini, D., Chan, H.-K., Crapper, J., Young, P.M., 2011. Particle aerosolisation and break-up in dry powder inhalers : evaluation and modelling of impaction effects for agglomerated systems. J. Pharm. Sci. 100 (7), 2744–2754.

Yang, R., Yu, A., Choi, S., Coates, M., Chan, H., 2008. Agglomeration of fine particles subjected to centripetal compaction. Powder Technol. 184 (1), 122–129.

Xu, H.M.T.M.Z., McLean, R., Langridge, J., Hickey, A.J., 2010. Dry powder aerosols generated by standardized entrainment tubes from drug blends with lactose monohydrate: 2. Ipratropium bromide monohydrate and fluticasone propionate. J. Pharm. Sci. 99 (8), 3415–3429.

Zheng, Z., Leung, S.S.Y., Gupta, R., 2021. Flow and particle modelling of dry powder inhalers: methodologies, recent development and emerging applications. Pharmaceutics 13 (2).